International Journal of Impact Engineering 77 (2015) 147–165

Contents lists available at ScienceDirect

International Journal of Impact Engineering

journal homepage: www.elsevier.com/locate/ijimpeng

High-speed digital imaging and computational modeling of dynamic failure in composite structures subjected to underwater impulsive loads

Siddharth Avachat, Min Zhou*

The George W. Woodruff School of Mechanical Engineering, School of Materials Science and Engineering, Georgia Institute of Technology, Atlanta, GA 30332-0405, USA

ARTICLE INFO

Article history:
Received 21 March 2014
Received in revised form
29 September 2014
Accepted 7 November 2014
Available online 20 November 2014

Keywords:
Underwater blast loading
High-speed digital imaging
Sandwich structures
Composite materials
Fluid–structure interaction
Computational modeling

ABSTRACT

The load-carrying capacity of composite structures under water-based impulsive loads is evaluated in relation to different core materials and load intensity. The analysis focuses on the role of core density and the effect of varying structural attributes and environmental conditions on deformation and failure mechanisms in monolithic as well as sandwich composites. The structures analyzed are simply supported planar composites with PVC foam cores and E-glass/vinylester facesheets. For the analysis carried out, the material properties of the sandwich cores are varied while the total mass is kept constant. The structures are subjected to impulsive loads of different intensities using a novel new projectile-impact-based facility called the Underwater Shock Loading Simulator (USLS). In-situ high-speed digital imaging and postmortem analysis are used to study the deformation and failure of individual components, focusing on the effects of loading intensities, failure modes and material heterogeneity. Depending on the loading rate, shear cracking and/or collapse are the primary failure modes of the polymeric foam cores. Core density and height also significantly influence the response and failure modes. On a per unit weight basis, structures with low density cores consistently outperform structures with high density cores because the former undergo smaller deflections, acquire lower velocities and transmit a smaller fraction of incident impulses. Scaling relations in the form of deflection and impulse transmitted as functions of core density and load intensity are obtained to provide guidance for structural design.

1. Introduction

Marine vessels operate in hostile environments which include high and low temperature extremes, transient dynamic loads like hull slamming, and corrosive sea water. Additionally, the structures are expected to withstand hydrodynamic loads resulting from surface and underwater explosions and weapons impact. Sandwich composites can provide good blast mitigation due to their high strength-to-weight ratios and high shear and bending resistances. The lightweight of sandwich composites can also improve speed and fuel economy. Compared with metal, composites are also more corrosion-resistant and have lower repair costs. These attributes make composite sandwich structures attractive materials for marine vessels. However, before such materials can be used, the relationships between their performance, constituent materials and geometric design must be well-understood and quantified.

Investigations have been out on the dynamic deformation and failure of layered materials. Results showed that key damage mechanisms include matrix cracking, fiber breakage and interlaminar delamination. The primary driving forces for the damage processes are transverse shear stresses [1–3]. Interlaminar delamination is the most detrimental to stiffness and strength and, therefore, is a major concern because delamination is not visible on the surface. Chang and co-workers [4–6] have studied the damage behavior of composite laminates under low velocity impact loading, concluding that in-ply matrix cracking precedes delamination growth and shear and bending crack initiation. The damage behavior of composite laminates is significantly influenced by matrix material, composite layup and geometric aspects such as size, thickness and loading area [7–9]. Minnaar and Zhou [10] used a novel interferometric experimental setup to show that interlaminar crack speeds are significantly higher under shear loading, and that crack speeds are strongly influenced by loading rate in mode II.

* Corresponding author. Tel.: +1 404 894 3294; fax: +1 404 894 0186.
E-mail address: min.zhou@gatech.edu (M. Zhou).

http://dx.doi.org/10.1016/j.ijimpeng.2014.11.008
0734-743X/

However, only limited study has been reported [11,12] on the dynamic response of composites to water-based impulsive loads. The compressive response and fracture behavior of core material are of primary importance in the structural response of sandwich structures. The stress–strain behavior of cellular foams at high strain rates has been investigated using Split Hopkinson Pressure Bar apparatuses [13–17]. These experiments reveal that PVC foams have mild strain rate sensitivity in the strain rate range of $\dot{\varepsilon} = 10^{-2}$ to 10^{3} s^{-1} and negligible strain rate sensitivity in the strain rate range of $\dot{\varepsilon} = 10^{-4}$ to 10^{-2} s^{-1}. The primary mechanism for energy absorption in foam cores is local wall collapse and volumetric, stress-saturated compression. Constitutive models for foams often rely on homogenized continuum descriptions of the cellular materials [18,19].

Through the combination of a thick, low-density core and thin facesheets, sandwich structures achieve considerably high shear and bending stiffness to weight ratios than homogenous plates of equivalent mass made exclusively of either the core or the facesheet material. The primary factors that influence the structural response of a sandwich structure are (1) facesheet thickness, (2) core thickness, and (3) core density. Previous research on the dynamic behavior of sandwich composites has focused on low velocity contact-based loads such as drop weight and projectile impact [13,14,20–24]. It is found that the overall deflection experienced by sandwich plates is significantly lower than monolithic plates of equivalent mass [25–33]. Additionally, the forces and impulses transmitted by sandwich structures are also smaller than those by monolithic structures [25,28,29]. Recent assessments of blast-loaded structures show that FSI (fluid–structure interaction) effects play an important role in dynamic response and can be exploited to improve the blast mitigation capability of marine structures [29,34–37]. Experiments focusing on different core topologies and specimen sizes have been carried out by Espinosa and co-workers [38–40] and McShane et al. [41] using underwater pressure impulses generated by gas gun impact and by Dharmasena et al. [42] using planar pressure impulses generated by explosive sheets. Shukla and co-workers [43–47] examined the dynamic response of sandwich structures consisting of woven E-glass composite facesheets and stitched core to air-based shock loading and concluded that stitched cores exhibit superior mechanical performance.

The deformation and failure of composite sandwich structures subjected to underwater impulsive loads are complicated due to competing damage mechanisms, failure modes, interfacial effects and material heterogeneity. The material properties of the different components significantly affect the blast resistance of the structures. In addition, loading (intensity, boundary conditions, and environments) influences the failure modes. Despite recent advances in understanding the dynamic response of sandwich composites, several issues remain. One is the lack of design relations that quantify the response as functions of both materials and geometric parameters. To obtain such relations, experiments that account for proper loading conditions are required. Diagnostics that provide in-situ, time-resolved response measurements are also required. Until recently, such experiments remained unavailable. Full scale underwater blast experiments have been carried out by Dear and co-workers using C4 explosives to generate the impulsive loads and high-speed photography with Digital Image Correlation (DIC) to evaluate the dynamic response of composite structures [48,49]. Nurick and co-workers have conducted air-blast experiments using PE4 plastic explosive and a ballistic pendulum apparatus to analyze the damage and energy dissipation in monolithic composite laminates and fiberglass/PVC foam sandwich structures [50,51].

The objective of the present study is to characterize the damage response of sandwich composites with different core densities but similar total masses. The focus of this analysis is on understanding the deformation and failure mechanisms, and quantifying the damage in composite structures as a function of structural attributes, material properties, loading conditions and loading rates. The loading of interest is high intensity water-based impulsive loads. Planar impulses resembling those resulting from underwater explosions are generated using the Underwater Shock Loading Simulator (USLS), a novel experimental setup developed recently. The USLS consists of a projectile-impact-based impulsive loading system, a water chamber, a target holder, and a safety enclosure. The target holder allows clamped and simply-supported boundary conditions. The experiments are designed to quantify the resistance of each structural configuration to underwater impulsive loads The response and failure mechanisms studied include overall deflection, face wrinkling, core–face debonding, core compression, core shear cracking and rupture. Of particular interest is the influence of load intensity and sandwich core characteristics on deformation and failure.

This is a combined experimental and computational study. Finite element simulations are carried out, accounting for the experimental conditions and material properties which are measured independently. The simulations also account for the fluid–structure interaction (FSI) effect at the water–composite interface. Failure mechanisms considered include shear cracking and fragmentation in the core, cracking in the facesheets, and core–face interfacial debonding. The simulations focus on damage initiation and evolution in the early stage of deformation (~1000 μs) since the load-carrying capacity is most critically reflected then. This combined experimental and numerical approach enables the identification of factors that play important roles in determining the dynamic response of the materials. The analysis uses metrics such as deflection, energy absorbed and impulse transmitted to quantify blast resistance. The results are presented in normalized forms to identify underlying trends in material and structural response.

2. Water-based impulsive loading experiments

Gas gun impact has been successfully used to generate impulsive loading through water [39,52–55]. To obtain controlled loading and simulate different water–structure contact conditions, the Underwater Shock Loading Simulator (USLS) was designed to provide a variety of load configurations with quantitative diagnostics. Important features of this facility include the ability to generate water-based impulsive loading of a wide range of intensity, the ability to simulate the loading of submerged structures, and integrated high-speed photographic and laser interferometric diagnostics. Fig. 1 shows a photograph of the USLS. The shock tube is an

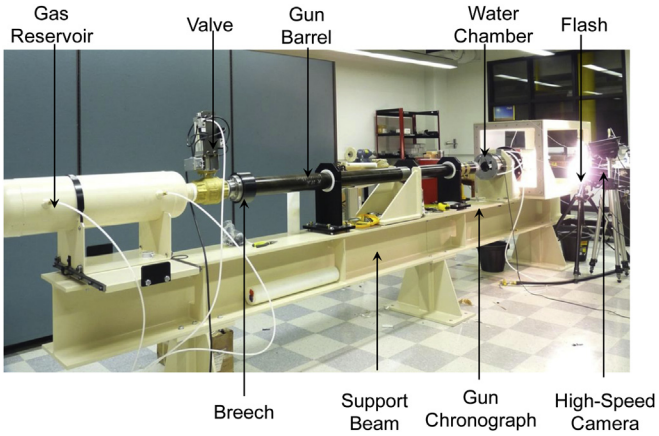

Fig. 1. Photograph of the Underwater Shock Loading Simulator (USLS). Pictured are the gas reservoir, gun barrel, water chamber and the Imacon 200D high-speed camera.

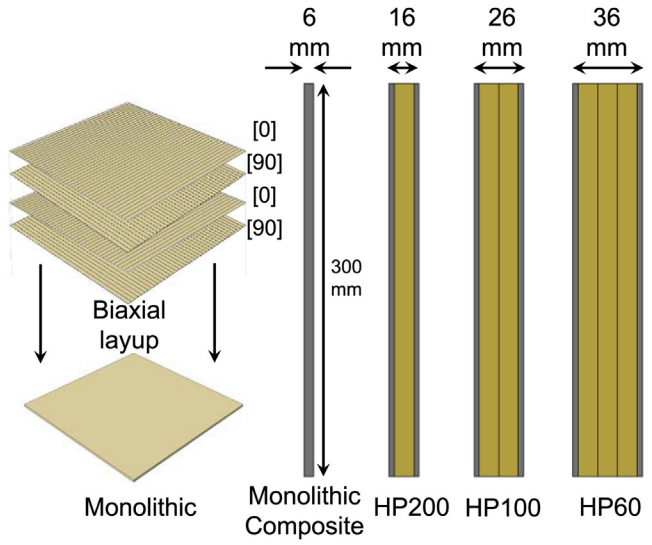

Fig. 2. Schematic illustration of sandwich structure with length L, core thickness T_C, and front and backface thickness T_F.

800 mm long cylinder which is horizontally mounted and filled with water. It is made of steel and has an inside diameter of 80 mm. A thin piston plate is mounted at the front end and the specimen is located at the rear end. A projectile is accelerated by the gas gun and strikes the piston plate, generating a planar pressure pulse in the shock tube. The impulsive load that impinges on the target induces deformation in the specimen at strain rates up to 10^4 s^{-1}. Projectile impact velocities in the range of 40–115 m s^{-1} are used to delineate the effect of loading rate on the deformation and failure behavior of the structures analyzed. This velocity range corresponds to peak pressures between 40 and 180 MPa, which are comparable to pressures observed in underwater explosions [56,57].

The experiments are designed to allow analyses of the onset and progression of core cracking, core–face debonding and delamination due to transverse impulse loading. Fig. 3(a) and (b) show the simply supported configuration with air-backed and water-backed conditions, respectively. In all the experiments reported here, a simply-supported beam configuration is used which creates maximum tensile and compressive stresses at the midpoint of the specimen. Additionally, it bears resemblance to the conditions created by hull stiffeners in naval vessels. The impulsive waves are planar and produce a uniform pressure over the contact area with the specimen, simplifying the deformation and failure in the material to a 2-D event.

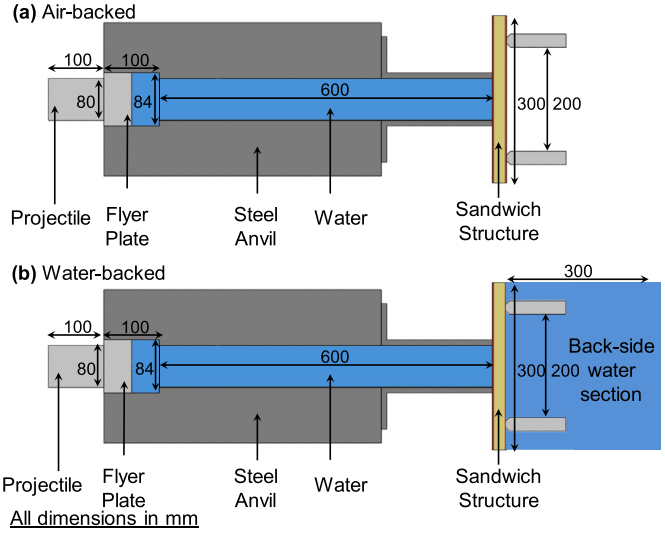

Fig. 3. Schematic illustration of the USLS and simply-supported sandwich structure in (a) air-backed and (b) water-backed configurations.

According to Taylor's analysis of one dimensional blast waves [58] impinging on a free standing plate, the pressure in the fluid at a fixed position follows the relation

$$p(t) = p_0 \exp\left(-\frac{t}{t_0}\right), \tag{1}$$

where p_0 is the peak pressure, t is time and t_0 is the decay time. The area under this curve is the impulse imparted by the wave

$$I = \int_0^t p(t)\,\mathrm{d}t. \tag{2}$$

A non-dimensionalized impulse $\bar{I}$ can be expressed as

$$\bar{I} = \frac{I}{\rho_w c_w \sqrt{A}}, \tag{3}$$

where ρ_w is the density of water, c_w is the speed of sound water in water and A is the area of loading. Impulsive waves due to underwater blasts have a characteristic decay time on the order of ~10^4 s. The experimental facility and numerical modeling simulate the effects of different standoff distances from an explosive source. In experiments involving explosives, Tri Nitro Toluene (TNT) is used to generate underwater blasts. Swisdak [56] showed that for an underwater explosion, the peak pressure (in MPa) scales as

$$p_0 = 52.4\left(\frac{M^{1/3}}{r}\right)^{1.13}, \tag{4}$$

where p_0 is the mass of TNT in kilograms and r is the standoff distance in meters. In the experiments reported here, pressures ranging from 10 MPa to 300 MPa can be generated using different projectile velocities. The impulses are measured using high dynamic range piezoelectric pressure transducers (#109C11 manufactured by PCB Inc.) and a high-frequency data acquisition system from National Instruments Inc. (NI-4432). Fig. 4(a)–(d) shows the comparison of experimentally measured and numerically calculated pressure histories corresponding to four different projectile velocities. The rise time of the pressure pulses is on the order of 25 μs and the decay time is on the order of 800 μs. The impulsive loads considered in this set of calculations have peak pressures of 40, 90, 140, 175, and 245 MPa which approximately correspond to 100 kg of TNT detonating at distances of 5.8, 2.83, 1.9 and 1.5 m respectively. The incident impulse magnitudes calculated using (2) are $I = \int_0^t p(t)\mathrm{d}t = 0.11$, 0.228, 0.359 and 0.424 kPa s. The normalized impulse magnitudes calculated using eqn. (3) are $\bar{I} = 0.015$, 0.035, 0.055 and 0.065, respectively.

3. Materials and panel construction

The facesheets are made of biaxial E-glass/vinylester composites and the core is PVC foam manufactured by DIAB Inc. [61]. Three PVC foam densities are used: 60, 100 and 200 kg/m^3. The sandwich structures analyzed here are in the form of beam specimens 300 mm in length and 80 mm in width. The four different specimen designs are as follows:

1. Composite monolithic panel consisting of biaxially oriented [(0/90/0/90)$_S$] glass fabric infiltrated with West System 105 epoxy resin. The panel thickness is 6 mm.

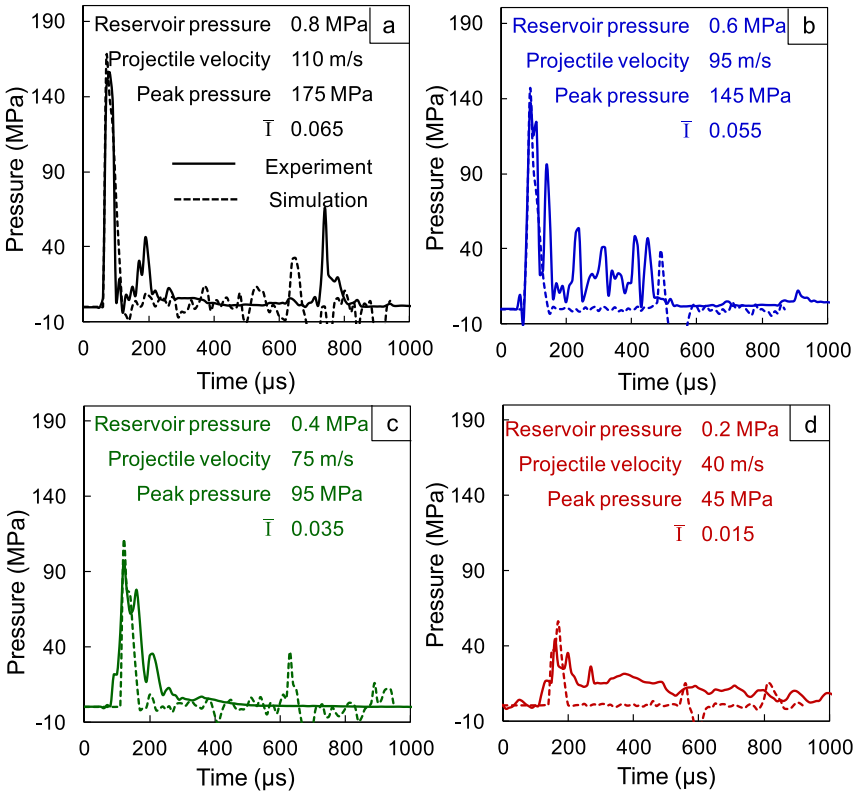

Fig. 4. Experimentally measured and numerically calculated pressure histories in the water chamber for four different projectile velocities and impulse magnitudes $\bar{I} = 0.015, 0.035, 0.055$ and 0.065.

2. Sandwich structure with glass fiber reinforced facesheets of thickness 2.5 mm and Divinycell HP60 core with a thickness of 30 mm for a total thickness of 35 mm.
3. Sandwich structure with glass fiber reinforced facesheets of thickness 2.5 mm and Divinycell HP100 core with a thickness of 20 mm for a total thickness of 25 mm.
4. Sandwich structure with glass fiber reinforced facesheets of thickness 2.5 mm and Divinycell HP200 core with a thickness of 10 mm for a total thickness of 15 mm.

The facesheets and cores are bonded together using the West System 105 epoxy resin and hardener. The four designs considered in this analysis have similar areal masses. Fig. 2 illustrates the makeup of composite structures analyzed. This sample size is approximately one order of magnitude smaller than composite sections used in ships. To compare the effects of different core densities on response, a relative density defined as

$$\bar{\rho} = \frac{\rho_{core}}{\rho_{PVC}} \tag{5}$$

is used. For the monolithic composite (which does not have a PVC foam core), the relative density is calculated by

$$\bar{\rho} = \frac{f_{matrix} \cdot \rho_{matrix}}{f_{fiber} \cdot \rho_{fiber}}, \tag{6}$$

where f_{matrix} and ρ_{matrix} are the volume fraction and density of the matrix, respective, and f_{fiber} and ρ_{fiber} are the volume fraction and density of the reinforcement, respectively. In a large naval structure, such as a ship or a submarine, structural components are in different service environments and are subject to different loading conditions. For example, ship hulls and superstructures are in contact with water on the outer side (impulse side) and air on the inner side. On the other hand, the keel, rudder, propeller blades and underwater pipelines are in contact with water on both sides (the impulse side and the protected side). For the purpose of the current study, the former is called the air-backed configuration [Fig. 3(a)] and the latter is called the water-backed configuration [Fig. 3(b)]. The different composite structures and the corresponding geometrical dimensions and areal masses are presented in Table 4.

4. Numerical model

4.1. Modeling of water–structure interaction

A number of approaches have been used to simulate the interactions of blast waves with structures, both in air and underwater. One approach is to simulate the fluid with Eulerian meshes and the solid structure with Lagrangian meshes. The behavior of the fluid in the Eulerian domain can be modeled using an equation of state. This technique is termed the "Arbitrary Lagrangian Eulerian" method and is often used to simulate the fluid structure interactions when large mesh distortions in the fluid domain are a major concern [62,63]. The second approach is to prescribe an exponentially decaying pressure on one face of the structure [64,65]. The incident impulse can be calculated using ConWep, a blast simulation code developed by the U.S. Army Corps of Engineers [66], which allows the impulse to be determined for a known explosive charge and the standoff distance between the charge and the target. A third approach is to simulate both the fluid and the structure with Lagrangian elements [67]. An appropriate equation of state is chosen to govern the response of the fluid. In this study, the third approach of a Lagrangian formulation for both the fluid and the structure is employed.

A Lagrangian formulation is adopted to simulate blast wave propagation in water. It captures the exponentially decaying

Table 1
Material properties for DIAB Divinycell HP core materials.

Parameter	Unit	HP60	HP100	HP200
Density	kg m^{-3}	65	100	200
Tensile modulus	MPa	20	100	250
Tensile strength	MPa	1.8	3.5	7.1
Compressive modulus	MPa	74	135	310
Compressive strength	MPa	0.95	2.0	5.4
Shear modulus	MPa	20	33	73
Shear strength	MPa	0.85	1.6	3.5
Fracture energy	kJ m^{-2}	0.10	0.32	0.81

pressure waves and cavitation at the fluid structure interface. The response of water is described by the Mie–Gruneisen equation of state such that

$$p = \frac{\rho_0 c_0^2 \eta}{(1 - s\eta)^2}\left(1 - \frac{\Gamma_0 \eta}{2}\right) + \Gamma_0 \rho_0 E_m, \tag{7}$$

where p is the pressure, c_0 is the speed of sound, ρ_0 is the initial density, E_m is internal energy per unit mass, Γ_0 is Gruneisen's gamma at a reference state, $s = \mathrm{d}U_s/\mathrm{d}U_p$ is the Hugoniot slope coefficient, U_s is the shock wave velocity, and U_p is the particle velocity which is related to U_s through a linear Hugoniot relation

$$U_S = c_0 + sU_p. \tag{8}$$

The parameters for the Mie–Gruneisen equation of state are listed in Table 3.

The interaction between the water and structure is effected by tying the nodes in the water to the corresponding nodes of the structure, thereby ensuring continuity of displacements. Three tie constraints are employed here, viz., (1) between the piston and water, (2) between the water and the walls of the water-chamber, and (3) between water and the composite structure.

4.2. Constitutive and damage models for composite laminates

A finite-deformation framework is adopted to account for large deformations in the composite. Linear orthotropic elastic constitutive behavior is assumed. Damage initiation and failure of each composite ply are captured with Hashin's damage model [11,68]. This is a homogenized model so that individual fibers and fiber–matrix interfaces are not modeled explicitly. Rather, the model provides a phenomenological representation of the different damage modes in composite structures. This framework incorporates four damage mechanisms: (1) matrix damage in tension, (2) matrix damage in compression, (3) fiber damage in tension, and (4) fiber damage in compression. The damage criteria for these mechanisms use the following parameters,

Table 2
Material properties for facesheets.

Parameter	Symbol	Unit	Value
Density	ρ	kg m^{-3}	1850
Tensile modulus	E_{11}	MPa	39,000
Transverse modulus	E_{22}	MPa	11,500
Shear modulus	G	MPa	3500
Longitudinal tensile strength	T_{11}	MPa	1200
Longitudinal compressive strength	C_{11}	MPa	620
Transverse tensile strength	T_{22}	MPa	50
Transverse compressive strength	C_{22}	MPa	128
Longitudinal shear strength	S_{12}, S_{21}	MPa	89
Transverse shear strength	S_{23}	MPa	60
Fracture energy for matrix in tension	G^c_{mt}	kJ m^{-2}	2
Fracture energy for matrix in compression	G^c_{mc}	kJ m^{-2}	2
Fracture energy for fiber in tension	G^c_{ft}	kJ m^{-2}	35
Fracture energy for fiber in compression	G^c_{fc}	kJ m^{-2}	35

Table 3
Parameters for the Mie–Gruneisen equation of state for water.

Parameter	Unit	Value
Density of water	kg m^{-3}	1000
Speed of sound in water	m s^{-1}	1482
Gruneisen's gamma	–	0.1

(1) matrix tension ($\hat{\sigma}_{22} \geq 0$):

$$F_m^T = \left(\frac{\hat{\sigma}_{22}}{T_{22}}\right)^2 + \left(\frac{\hat{\tau}_{12}}{S_{12}}\right)^2, \tag{9}$$

(2) matrix compression ($\hat{\sigma}_{22} < 0$):

$$F_m^C = \left(\frac{\hat{\sigma}_{22}}{2S_{23}}\right)^2 + \left(\frac{\hat{\tau}_{12}}{S_{12}}\right)^2 + \left[\left(\frac{C_{22}}{2S_{23}}\right)^2 - 1\right]\frac{\hat{\sigma}_{22}}{C_{22}}, \tag{10}$$

(3) fiber tension ($\hat{\sigma}_{11} \geq 0$):

$$F_f^T = \left(\frac{\hat{\sigma}_{11}}{T_{11}}\right)^2 + \left(\frac{\hat{\tau}_{12}}{S_{12}}\right)^2, \text{ and} \tag{11}$$

(4) and fiber compression ($\hat{\sigma}_{11} < 0$):

$$F_f^C = \left(\frac{\hat{\sigma}_{11}}{C_{11}}\right). \tag{12}$$

In the above expressions, subscript "11" denotes the longitudinal direction and subscript "22" denotes the transverse direction, E, T and C are the tensile modulus, tensile strength and compressive strength, respectively. The in-plane/longitudinal shear strengths are $S_{12} = S_{31}$ while the out-of-plane/transverse shear strength is S_{23}. In addition, $\hat{\sigma}_{11}, \hat{\sigma}_{22}$ and $\hat{\tau}_{12}$ are components of the effective stress tensor in the form of $\hat{\boldsymbol{\sigma}} = \boldsymbol{M}\boldsymbol{\sigma}$, with $\boldsymbol{\sigma}$ being the nominal stress tensor and $\boldsymbol{M}$ being the damage operator given by

$$\boldsymbol{M} = \begin{bmatrix} 1/\left(1 - D_f\right) & 0 & 0 \\ 0 & 1/(1 - D_m) & 0 \\ 0 & 0 & 1/(1 - D_s) \end{bmatrix}, \tag{13}$$

where D_f, D_m, and D_s are damage variables in fibers, matrix and associated with the shear modes, respectively [69].

In eqs. (9)–(12), for each parameter, a value of less than 1.0 indicates no damage and a value of 1.0 indicates damage. The upper bound to all damage variables in an element is $D_{max} = 1$. Prior to damage initiation, the material is linear elastic. After damage initiation, the response of the material follows

$$\boldsymbol{\sigma} = \mathbf{C}_\mathrm{d}\boldsymbol{\varepsilon}, \tag{14}$$

where $\boldsymbol{\varepsilon}$ is the strain and $\mathbf{C}_\mathrm{d}$ is the elasticity matrix accounting for damage in the form of

Table 4
Experiment schedule. The thicknesses of the facesheets are varied to maintain similar areal masses in the composite structures.

Beam designation	Core density (kg m^{-3})	Core thickness (mm)	Facesheet thickness (mm)	Areal mass (kg m^{-2})
M 1,2,3,4	–	–	6	10.5
HP60 1,2,3,4	60	30	3	10.7
HP100 1,2,3,4	100	20	3	10.9
HP200 1,2,3,4	200	10	3	10.9

$$\mathbf{C}_{\mathrm{d}} = \frac{1}{D}\begin{bmatrix} \left(1-D_f\right)E_{11} & \left(1-D_f\right)(1-D_m)\upsilon_{21}E_{11} & 0 \\ \left(1-D_f\right)(1-D_m)\upsilon_{12}E_{22} & (1-D_m)E_{22} & 0 \\ 0 & 0 & (1-D_m)\mu D \end{bmatrix}. \tag{15}$$

In the above relation, $D = 1-(1-D_f)(1-D_m)\upsilon_{12}\upsilon_{21}$, D_f reflects the current state of fiber damage, D_m reflects the current state of matrix damage, D_s reflects the current state of shear damage, E_{11} is the Young's modulus of the composite in the fiber direction, E_{22} is the Young's modulus of the composite in the transverse directions, μ is the shear modulus, υ_{12} and υ_{21} are Poisson's ratios. The components of the damage variables are

$$\left.\begin{aligned} D_f &= \begin{cases} D_f^t, \text{ fiber tensile damage variable,} \\ D_f^c, \text{ fiber compressive damage variable,} \end{cases} \\ D_m &= \begin{cases} D_m^t, \text{ matrix tensile damage variable,} \\ D_m^c, \text{ matrix compressive damage variable, and} \end{cases} \\ D_s &= 1-\left(1-D_f^t\right)\left(1-D_f^c\right)(1-D_m^t)(1-D_m^c). \end{aligned}\right\} \tag{16}$$

D_f^t, D_f^c, D_m^t, and D_m^c are calculated using $G_{mt}^c, G_{mc}^c, G_{ft}^c$ and G_{fc}^c which are fracture energies associated with matrix tension and compression and fiber tension and compression, respectively. The material properties used in these calculations were obtained from Refs. [22,40,70–73] and are listed in Table 2.

4.3. Constitutive and damage models for PVC foams

The PVC foam core used in the experiments is Divinycell HP with densities of 60, 100 and 200 kg/m^3 [74]. The Deshpande and Fleck crushable foam plasticity model [75] is used to describe the constitutive behavior of PVC foams. In this model, the yield surface for volumetric hardening is defined as

$$F = \sqrt{q^2+\alpha^2(p-p_0)^2} - B = 0, \tag{17}$$

where p is the pressure stress, q is the von Mises stress, $\alpha = B/A$ is the shape factor of the yield ellipse that defines the relative magnitude of the axes. B is the size of the q-axis of the yield ellipse and A is the size of the p-axis of the yield ellipse. The shape factor is specified by

$$\alpha = \frac{3k}{\sqrt{(3k_t+k)(3-k)}}, \quad \text{where } k = \frac{\sigma_c^0}{p_c^0} \text{ and } k_t = \frac{p_t}{p_c^0} \tag{18}$$

where σ_c^0 is the initial yield stress in uniaxial compression, p_c^0 is the initial yield stress in hydrostatic compression and p_t is the yield strength in hydrostatic tension. The uniaxial stress–strain response of the foam is adapted from Tagarielli et al. [15] and is shown in Fig. 5. Material parameters for the PVC foams are provided by the manufacturer and listed in Table 1.

Experiments performed show that fracture and fragmentation are significant damage mechanisms in composite sandwich structures subjected to underwater impulsive loads. A phenomenological damage criterion proposed by Hooputra et al. [76] is implemented to predict the onset of rupture due to strain localization and to capture the subsequent fragmentation of the core material. The damage model assumes that the equivalent plastic strain at the onset of damage, $\bar{\varepsilon}_D^{pl}$, is a function of stress triaxiality and equivalent plastic strain rate, i.e.

$$\bar{\varepsilon}_D^{pl}\left(\eta, \dot{\bar{\varepsilon}}^{pl}\right), \tag{19}$$

where $\eta = -p/q$ is the stress triaxiality, p is the hydrostatic stress, q is the von Mises equivalent stress and $\dot{\bar{\varepsilon}}^{pl}$ is the equivalent plastic strain rate. The criterion for damage initiation is met when

$$\omega_D = \int \frac{\mathrm{d}\bar{\varepsilon}^{pl}}{\bar{\varepsilon}_D^{pl}\left(\gamma, \dot{\bar{\varepsilon}}^{pl}\right)} = 1, \tag{20}$$

where ω_D is a state variable that increases monotonically with plastic deformation. At each increment during the analysis the incremental increase in ω_D is computed as

$$\Delta\omega_D = \frac{\Delta\bar{\varepsilon}^{pl}}{\bar{\varepsilon}_D^{pl}\left(\eta, \dot{\bar{\varepsilon}}^{pl}\right)} \geq 0. \tag{21}$$

The evolution of damage is based on fracture energy per unit area to be dissipated during the damage process. The data for fracture toughness is obtained from experiments carried out by Poapongsakorn and Carlsson [77].

4.4. Water-tank, projectile, piston and supports

The water-tank and supports are made of stainless steel and the piston and projectiles are made of aluminum. Linear elastic constitutive behavior is assumed for these components. Non-penetrating, penalty contact interactions are specified between each of the components.

5. Structural design

Non-dimensional variables are used for quantitative evaluation of the dynamic response of the composite panels as a function of loading and structural attributes. In structural design, necessary performance requirements are specified and the structural

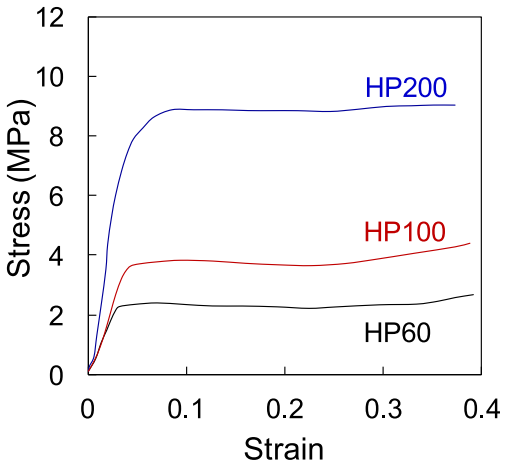

Fig. 5. Stress strain curves of HP60, HP100 and HP200 at a strain rate of ~1000 s^{-1} [15].

characteristics that fulfill these objectives are ascertained. The material attribute of particular interest here is the normalized relative density $\overline{\rho}$ and the loading intensity is the normalized incident impulse $\bar{I}$. These parameters are varied independently of each other and the performance of each structure is quantified using the normalized deflection Δ/L and transmitted impulse I_T. Based on the experiments and numerical simulations reported here, four material–structure–performance relations have been developed. These relations are in the form of a power law in the form of $z = [A \cdot \overline{\rho}^{(m)} \cdot \bar{I}^{(n)}],$, where z is the acceptable deflection and transmitted impulse levels and A, m and n are constants. These relations can be used to inform structural design with the understanding that they should only be used for the specified material, structural parameter ranges and loading conditions. For a given combination of deflection and impulse transmitted, the optimum value of relative density for a specific impulsive load level can be achieved by varying material properties of the monolithic plate or sandwich core.

6. Experimental results

6.1. Deformation modes and failure mechanisms

When the underwater impulsive wave impinges on the target, a number of deformation and failure modes are observed in the sandwich composite. Due to structural deflection and bending, the frontface experiences compressive loading which causes face wrinkling which is resisted by the core. Frontface buckling can ultimately lead to matrix cracking and fiber–matrix debonding followed by rupture. Failure in the frontface is followed by core compression, core shear cracking and fragmentation. Initially, the core undergoes rapid compression near the load region, a phenomenon called “core indentation”. Triantafillou and Gibson [78,79] showed that the indentation load is set by plastic yielding in the core and simultaneous inelastic deformation in the frontface. Since the facesheets in this set of experiments are relatively thin, it can be assumed that the core collapses at uniform shear strength with negligible additional strength provided by the facesheets. Due to the simply-supported loading configuration, the backface experiences maximum stresses near the midplane and fails under tensile loading. The interfaces between the core and facesheets are subjected to multi-axial loads due to the complicated deformation modes in both the facesheets and the core.

6.2. Effect of core density

Fig. 6 shows a sequence of high-speed digital images of a monolithic composite plate subjected to an underwater impulsive load in the USLS. The projectile velocity is 75 m s^{-1}, the peak pressure is 95 MPa and the resulting impulse corresponds to $\bar{I} = 0.035$ shown in Fig. 4(c). In addition to the water flowing out of the water-chamber, a thin Mylar film used for sealing the water-chamber can be seen to the left of the panel. The deformation can be divided into two regimes: (1) flexural wave propagation towards the supports and (2) structural deflection. The flexural wave travels towards the supports in a very short time (~50 μs). Although the resolution of the camera is sufficient to capture this phenomenon, we are more interested in structural response in the form of damage and out-of-plane deflection, which take place over a longer time span. Consequently, the temporal resolution of the camera is

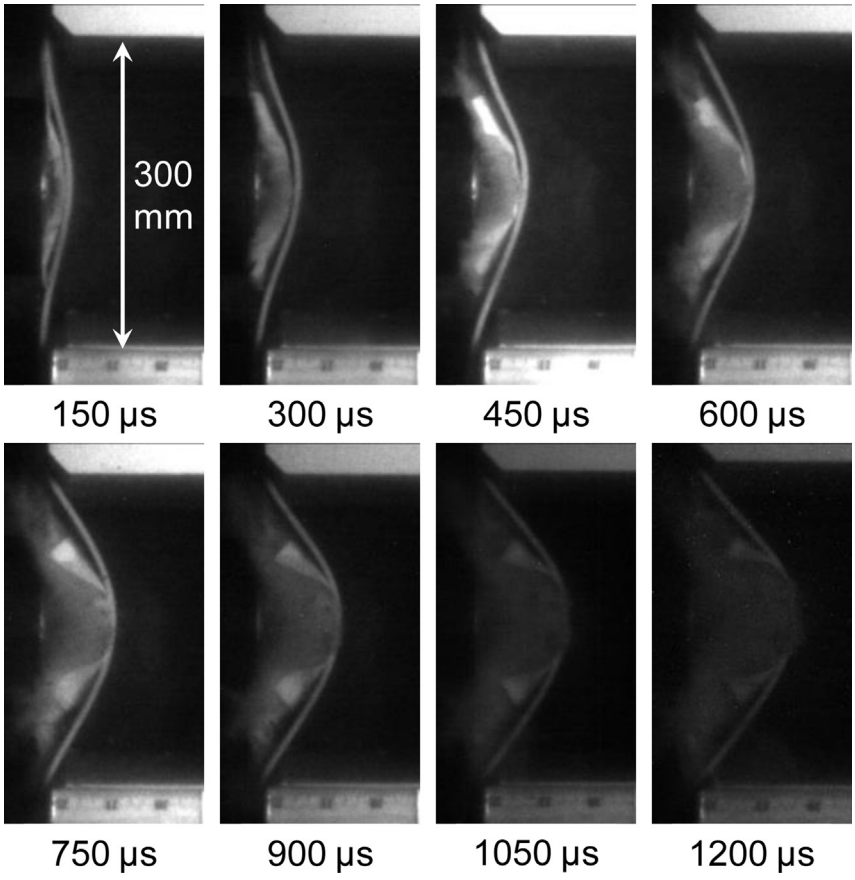

Fig. 6. Sequence of high-speed photographs showing the deformation in a monolithic composite plate subjected to underwater impulsive loading with $\bar{I} = 0.035$.

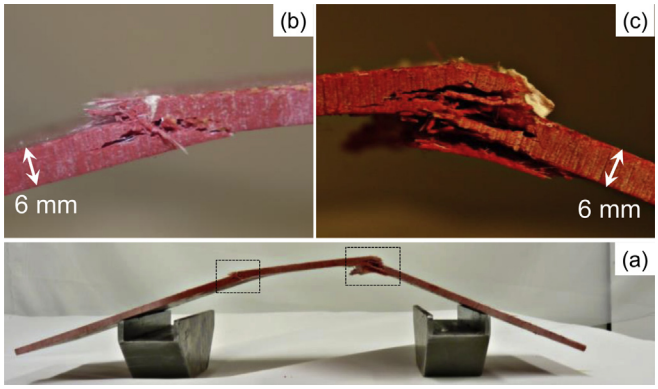

Fig. 7. Postmortem photographs of impulsively loaded composite plates with cross sections showing interlaminar delamination, matrix cracking, fiber matrix debonding, fiber pullout and intra laminar cracking.

selected to capture the behavior over a duration of 2 ms. The displacement of the backface is tracked at the midpoint and compared with that of other structures. Although the deformation and damage in sandwich structures can be tracked using high-speed digital imaging, the monolithic composite plate is quite thin and damage mechanisms are hard to discern from high-speed photographs. These damage mechanisms are revealed in post-mortem photographs of the monolithic composite plate shown in Fig. 7(a)–(c). Fig. 7(a) shows the deformed monolithic plate with clearly formed hinges near the load site which experiences the highest impulsive load. Fig. 7(b) and (c) shows delamination between successive layers in the laminate, matrix cracking, fiber pullout and rupture. While the deflection is relatively uniform over the length of the composite plate, damage mechanisms are predominantly observed near the circumference of the shock tube and near the supports, indicating significant influence of shear effects in damage creation.

Fig. 8 shows a sequence of high-speed photographs of a composite sandwich structure with a Divinycell HP200 core subjected to $\bar{I} = 0.035$ as shown in Fig. 4(c). Initially, flexural waves travel through the frontface, severing the core facesheet bond. In cases where the core facesheet bond is stronger than the PVC foam, a layer of core material is separated by the facesheet due to the low tensile strength of PVC foam. Core–face debonding and core failure due to cracking and fragmentation are observed at $t = 50$ μs. Core crushing commences at $t = 150$ μs and is restricted to the region close to the loading area. Core cracking and fragmentation occurs and the structure experiences complete failure at $t = 1200$ μs. Fig. 9 shows a sequence of high-speed photographs of a composite sandwich structure with a Divinycell HP100 core subjected to $\bar{I} = 0.035$. Core––facesheet debonding and frontface wrinkling failure occur at $t = 50$ μs followed by core indentation at $t = 150$ μs. In core indentation failure, the core material fails in a highly localized region, leading to compressive stresses in the frontface which cause frontface buckling. The damage mechanisms in the frontface for this type of deformation are in the form of fiber rupture and matrix cracking. Shear dominated cracks originate near the supports at $t = 300$ μs followed by core cracking $t = 900$ μs. This structure does not experience rupture.

Fig. 10 shows a sequence of high-speed photographs of a composite sandwich structure with a Divinycell HP60 core subjected to $\bar{I} = 0.035$. The response of the sandwich structure with an HP60 core is quite different from those with HP100 or HP200 cores in that

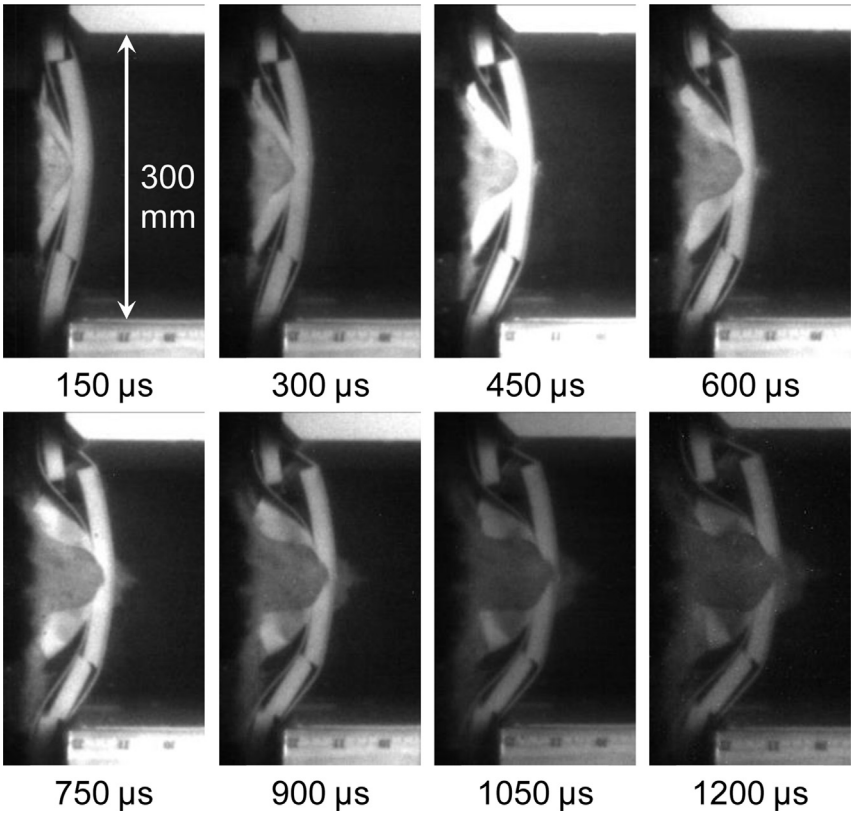

Fig. 8. Sequence of high-speed photographs showing the deformation in a sandwich structure with HP200 core subjected to underwater impulsive loading with $\bar{I} = 0.035$. Large scale core frontface debonding and core fragmentation can be observed. The core fractures prior to core compression and rupture occurs at $t = 900$ μs.

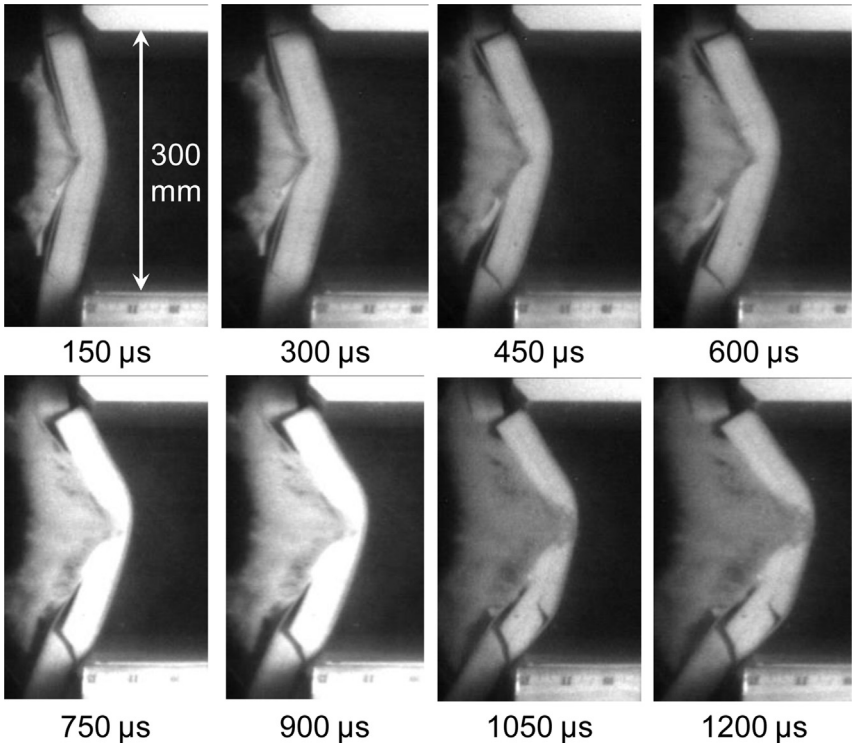

Fig. 9. Sequence of high-speed photographs showing the deformation in a sandwich composite with HP100 core subjected to underwater impulsive loading with $\bar{I} = 0.035$. Frontface wrinkling and core indentation occurs at $t = 300$ μs. Inclined cracks initiated at $t = 600$ μs and were followed by rupture at $t = 900$ μs.

there is no core shear cracking, frontface wrinkling and core face debonding. Core compression commences immediately after the onset of loading at $t = 150$ μs and inclined cracks originate near the loading circumference area. These cracks propagate from the frontface to the backface and branch into multiple cracks (at $t = 450$ μs) near the backface, causing core backface debonding. After core face debonding, core fragmentation initiates. Core compression and core cracking occur simultaneously with crack

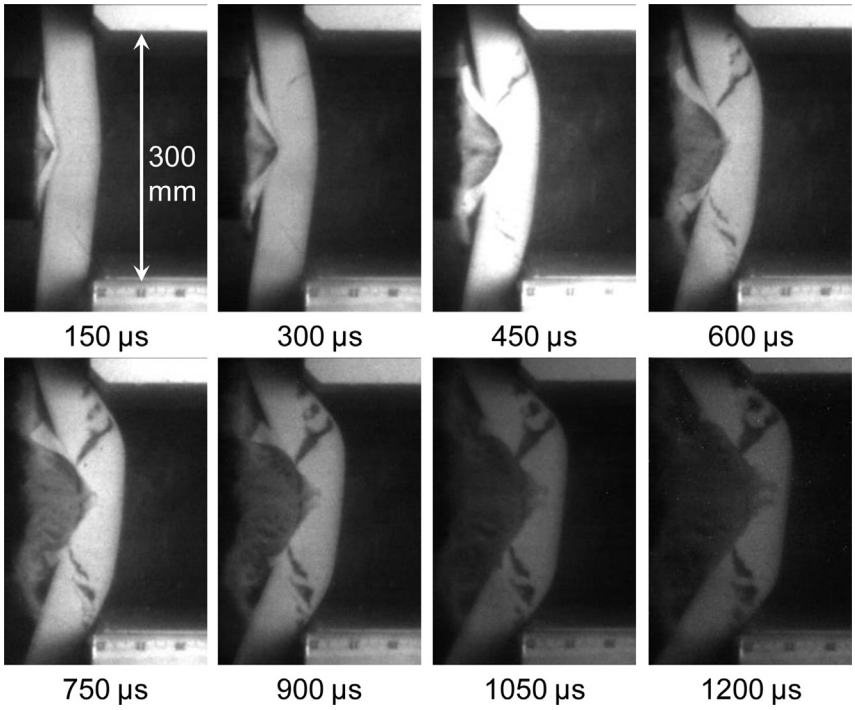

Fig. 10. Sequence of high-speed photographs showing the deformation in a sandwich composite with HP60 core subjected to underwater impulsive loading with $\bar{I} = 0.035$. Deformation in the core is quite uniform and bending deformation occurs prior to core cracking. Core face debonding is relatively less widespread and facesheet wrinkling does not occur.

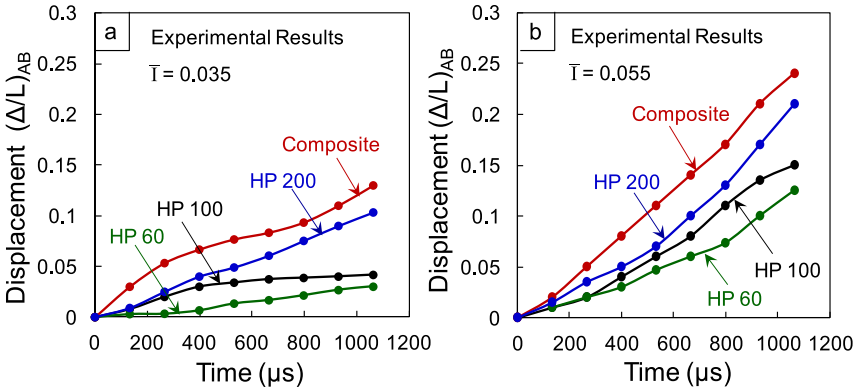

Fig. 11. Experimentally measured midpoint displacements as functions of time for sandwich structures subjected to (a) $\bar{I} = 0.035$ and (b) $\bar{I} = 0.055$.

propagation through the core. Core indentation (localized compressive failure) in HP60 cores occurs to a greater extent than HP100, primarily due to the fact that HP60 compresses at a much lower load than HP100. This indicates that there is a lower limit on core density for a blast-resistant structures. It should be noted that among all the structures studied here, HP60 is the only core for which no catastrophic failure is observed at any load intensity studied.

The midpoint deflections for each composite structure are shown in Fig. 11. The monolithic composite structure is used as a benchmark for comparison with sandwich structures. It is determined that the lower the deflection when compared to that of the monolithic composite plate at a particular time, the better is the blast resistance. Fig. 11(a) and (b) shows the normalized deflection Δ/L (where Δ is deflection and L is the span of the composite panel) of composite structures subjected to $\bar{I} = 0.035$ and $\bar{I} = 0.055$, respectively. A comparison of the initial slopes of the deflection vs. time plots shows that the structures with higher relative densities move most rapidly in the direction away from the impulsive load direction. As the loading rate increases, the rate of deflection also increases monotonically. The monolithic composite experiences the highest deflection at the highest rate compared with the sandwich structures. The sandwich structure with HP100 core initially exhibits a rate of deformation that is similar to the sandwich structure with HP200 core but the response of HP100 core diverges at $t = 400$ μs and the rate of deflection increase decreases. For the sandwich structure with HP60 core, the rate of deflection increase is the lowest among all three structures studied for both load intensities.

6.3. *Effect of load intensity*

The effect of loading rate on blast resistance is evaluated through a range of incident impulsive load intensities shown in Fig. 4. Fig. 12 presents a sequence of high-speed photographs showing the deformation in different composite structures subjected to $\bar{I} = 0.065$, which is the highest load intensity considered in this analysis. Fig. 12(a) shows the response of monolithic composite plate which is similar to what is seen in the high-speed photographs of a monolithic composite subjected to $\bar{I} = 0.035$ discussed earlier. The effect of load intensity is much more significant for sandwich structures due to the nature of the dynamic

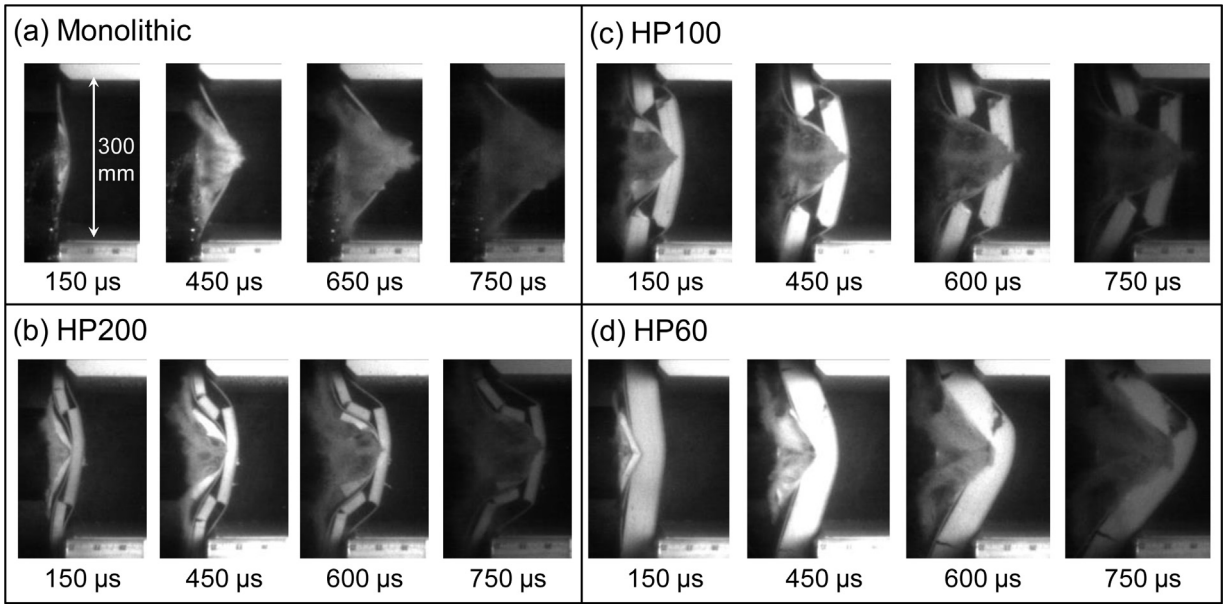

Fig. 12. Sequence of high-speed photographs showing the deformation in composite structures subjected to $\bar{I} = 0.065$. The impulse imparted to the frontface causes it to move away at a velocity higher than the allowable dynamic crush rate of the core resulting in large differential displacements which cause frontface fracture and core cracking, but relatively low core compression.

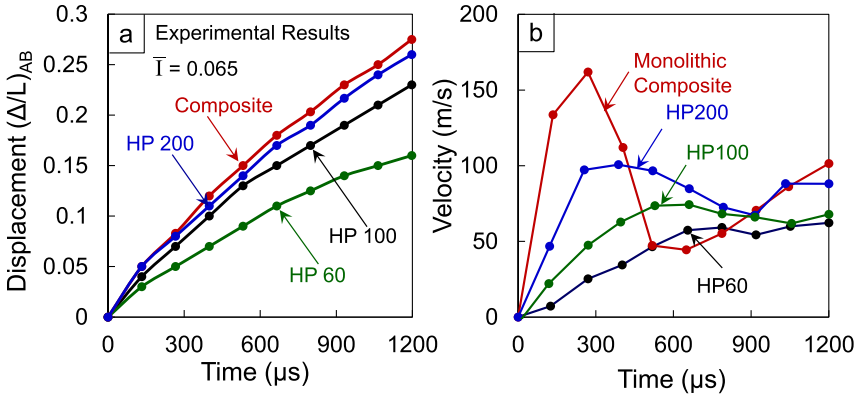

Fig. 13. Experimentally measured midpoint displacements and velocities as functions of time for sandwich structures subjected to $\bar{I} = 0.065$.

behavior of the core materials. Fig. 12(b) shows the response of a sandwich structure with HP200 core subjected to $\bar{I} = 0.065$. The core fractures in a direction perpendicular to the planar wave and causes considerable core–face debonding in both the front and the back interfaces. Core compression is negligible and fragmentation is observed near the supports. Fig. 12(c) shows the behavior of a sandwich structure with HP100 core. The HP100 core fractures at an inclined angle from the loading direction and simultaneously undergoes core compression and crushing. The response of a sandwich structure with an HP60 core is shown in Fig. 12(d). Core compression and frontface wrinkling are observed at $t = 150$ μs. Core indentation occurs at $t = 300$ μs and the core starts to crack at $t = 450$ μs. Damage and deformation in the sandwich structure with an HP60 core is significantly lower than those in other composite structures. At high load intensities, it appears that the impulse imparted to the frontface causes it to move away at velocities higher than the allowable dynamic crush rate of the core, resulting in large differential displacements which cause frontface fracture and core cracking, but negligible core compression. Fig. 13a shows the midpoint displacements as functions of time for the four different structures. The sandwich structures with HP200 and HP100 cores and the monolithic structures show relatively similar deformation histories reaching a Δ/L value of 0.25 at approximately the same rate. The sandwich structure with HP60 cores shows superior blast mitigation, deflecting at a lower rate and reaching a Δ/L value of 0.17, which is ~60% of that for the other sandwich structures.

The results show that core density and load intensity profoundly affect both the rate and the extent of deformation in the composite structures. The study indicates that structure with low density cores consistently outperform structures with high density cores of equal mass. Fig. 13b shows the backface velocity histories for all composite panels. The monolithic composite experiences the highest transverse velocities followed by sandwich structures with HP200, HP100 and HP60, in that order. This behavior can be explained by the presence of the sandwich core which reduces the velocity of the deforming composite panel. The lower the core density and thicker the core, the greater the reduction in velocity due to the ability of the core to undergo compression. Additionally, the variations in geometric parameters have an effect on flexural rigidity and deformation in sandwich panels. Since a fully dynamic computational framework is used to in this analysis, structural effects beyond bending, as well as bending, are captured.

Fig. 14 shows the normalized deflections $(\Delta/L)_{AB}$ for all 16 air-backed configurations as functions of impulse $\bar{I}$ and relative density $\bar{\rho}$. At all impulse magnitudes, structures with the lowest relative density experience the least deflections. The deflections increase with increasing relative density as well as impulse magnitudes. Structures with HP200 cores perform only marginally better than monolithic structures. Structures with the HP100 and HP60 cores exhibit significantly higher blast resistances in comparison to the structure with the HP200 core and the monolithic composite. The relationship between deflection in air-backed structures$(\Delta/L)_{AB}$, and $\bar{I}$ and $\bar{\rho}$ can be given by

$$(\Delta/L)_{AB} = 20 \cdot \bar{\rho}^{(0.62)} \cdot \bar{I}^{(1.20)}. \tag{22}$$

7. Computational results

7.1. Validation of numerical approach

A number of failure mechanisms are observed by time-resolved as well as post-mortem inspection of the composite panels. Failure in the monolithic composite panels consists of matrix cracking and fiber pullout, in addition to multiple delaminations through the cross-section. With increasing load intensity, the severity of matrix cracking increases significantly. In sandwich structures, the failure mechanisms consist of (1) matrix cracking, (2) fiber rupture, (3) fiber–matrix debonding, (4) permanent core compression and core indentation, (5) core shear cracking and rupture, (7) core–face debonding, and (8) rupture of the composite panel. The effects of loading rate are much more significant for sandwich composites with high density cores (HP100 and HP200) than for structures

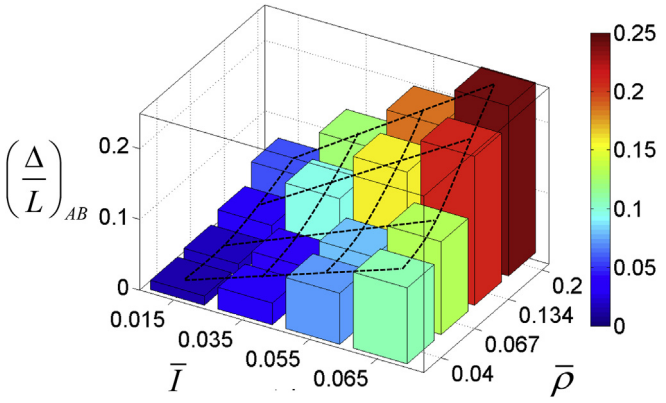

Fig. 14. Normalized deflections in air-backed structures as functions of normalized incident impulse $\bar{I}$ and normalized density $\bar{\rho}$. On a unit weight basis, low density cores consistently outperform high density cores. Sandwich structures are superior to monolithic composite plates at all impulse magnitudes.

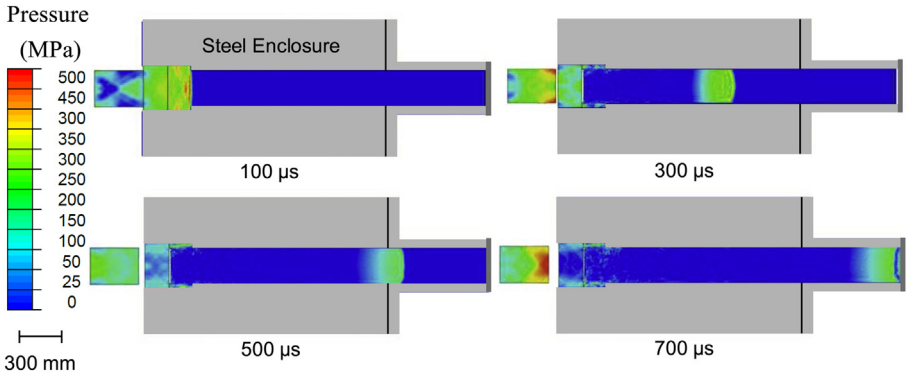

Fig. 15. Cross-sectional view of a finite-element simulation of the USLS showing the distributions of pressure for an impulsive wave generated in the water chamber when a projectile traveling at velocity 75 m s^{-1} strikes the piston plate.

with low density cores (HP60). Concurrent numerical analyses of the response of composite panels provide a more in-depth understanding of the structural response and failure mechanisms. Based on the experiments, a parametric finite element analysis is carried out, focusing on the effects of (i) load intensity, (ii) changes in relative density (monolithic, HP60, HP100, and HP200), and (iii) air-backed and water-backed loading conditions. For all the calculations presented, simply-supported boundary conditions are used, as in the experiments. Also as in experiments, four different projectile velocities are used to generate impulsive loads on the central area of the specimen. Fig. 4 shows a comparison of experimentally measured and numerically calculated pressure profiles in the USLS.

The deflection and impulse transmission in the monolithic plate are taken as benchmarks to which the deflection and impulse transmission in the sandwich structures are compared to gauge relative performance. Fig. 15 shows a sectional view of the pressure wave generated by a projectile traveling at 75 m s^{-1}. The peak pressure in this case is ~95 MPa. The Mie–Gruneisen equation of state provides an accurate representation of planar pressure pulses traveling through an incompressible medium. Fig. 16 shows a comparison of high-speed photographs from experiments and contour plots for damage from simulations at different times for a structure with the HP60 core subjected to $\bar{I} = 0.035$. The experiments reveal that core compression commences immediately after the onset of loading at $t = 150$ μs and inclined cracks originate near the loading circumference. These cracks propagate from the frontface to the backface and branch (at $t = 450$ μs) near the backface, leading to core–backface debonding. Core indentation is observed at the center, followed by core cracking and finally culminating in fragmentation and collapse. Although damage in the frontface is severe, the backface is relatively undamaged. The entire structure achieves a common velocity at $t = 600$ μs. The numerical

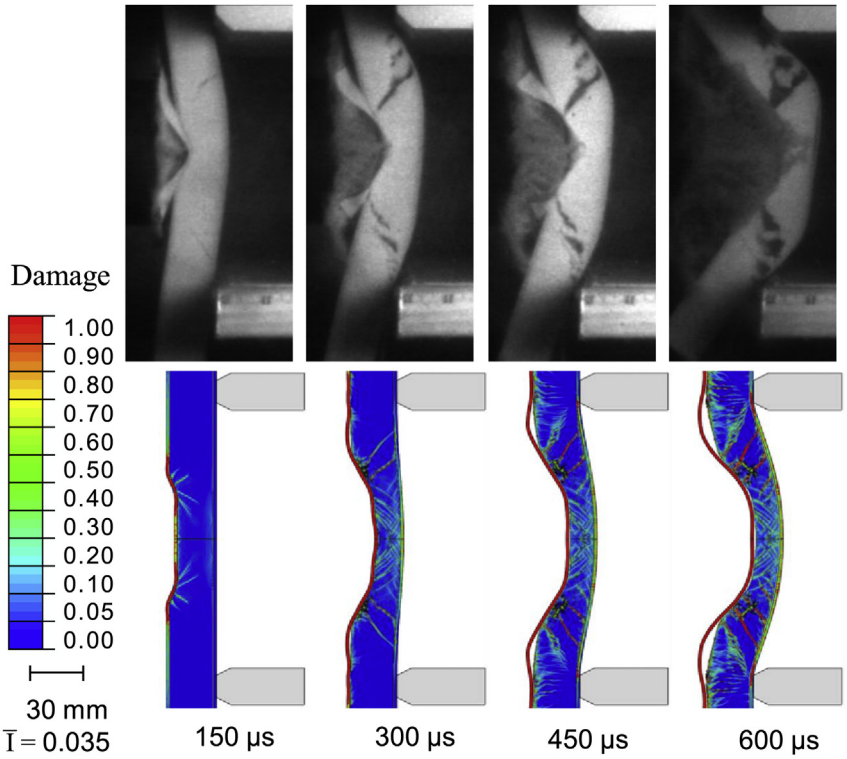

Fig. 16. Cross-sectional view showing a comparison of experimentally measured and numerically calculated deformation sequences for a sandwich structure with HP60 core subjected to $\bar{I} = 0.035$. The major deformation mechanisms (core cracking, core frontface debonding and core crushing) are captured in the finite element simulations.

simulations capture the different failure modes observed in the experiments. The major deformation modes captured can be divided into distinct regimes based on the time required for each regime: (1) load transfer through frontface and onset of core compression; (2) elastic and inelastic core compression; (3) core cracking and fragmentation and load transfer to backface; and (4) bending in entire structure. The material properties of the sandwich core determine the duration of each regime. The numerical simulations allow the identification of various damage mechanisms and the chronological sequence in which these mechanisms initiate. The overall panel deformation and core compression and core cracking closely resemble those observed in high-speed photographs of the experiments reported here. The magnified view of deformation sequences shows that initially, damage is much more severe near the loading area, and as the panel experiences further deformation, core shear and core–face debonding initiate. Strain localization observed in experiments is replicated in the numerical simulations in the form of cracks propagating outwards at ~45° to the loaded region. Extensive cracking and delamination are also observed in the backfaces.

The distributions of damage due to matrix cracking and core cracking and fragmentation in different composite structures are shown in Fig. 17(a)–(d) for $\bar{I} = 0.035$ at $t = 600$ μs. In the monolithic composite [Fig. 17(a)], matrix cracking is observed near the circumference of the loading area. Significant damage occurs in the composite layers that are in contact with water but the backface of the monolithic composite is relatively undamaged. For the sandwich composite with the HP200 core [Fig. 17(b)], core frontface and backface debonding occurs over the entire structure and the core fails through shear cracking. Both the frontface and the backface experience considerable damage. For the sandwich composite with the HP100 core [Fig. 17(c)], the frontface experiences significant damage and core frontface debonding is observed. For the sandwich composite with the HP60 core [Fig. 17(d)], frontface buckling and core frontface debonding are observed; but the backface is relatively undamaged. It is apparent that damage in the backface is highly dependent on the properties of the core. Damage and failure in simply supported sandwich structures occur primarily through the formation of discrete 45° core cracks and separation along the core face interface. Structural failure in all cases is due to shear stresses near the loading area and bending stresses near the supports. Results show reasonable agreement between the experiments and numerical simulations. The compressible foam constitutive model predicts the initial deformation response which is governed by the core compression. Additionally, the damage criterion provides an accurate characterization of damage creation and growth in the composite as well as foam components. However, the numerical model slightly overestimates the compressibility of the foam core, resulting in greater permanent core compression in the simulations as compared to experiments.

7.2. Deflection

Bending deformation initiates in the structure immediately after the onset of loading. In this configuration, the midpoint of the backface experiences the highest deflection and stresses. Fig. 18 shows the histories of center displacements normalized by the length of the structure for front and backfaces of the sandwich panels with the (a) HP60, (b) HP100, and (c) HP200 cores along with those of the monolithic composite of equivalent weight. The shaded region shows the core compression at the center. Results show that the center displacement of the monolithic composite is higher than those of all sandwich structures. The velocity acquired by the monolithic plate is very similar to that of the frontface in all three cases. For the three core densities, the frontface acquires much higher velocities than the backface. Therefore, the load

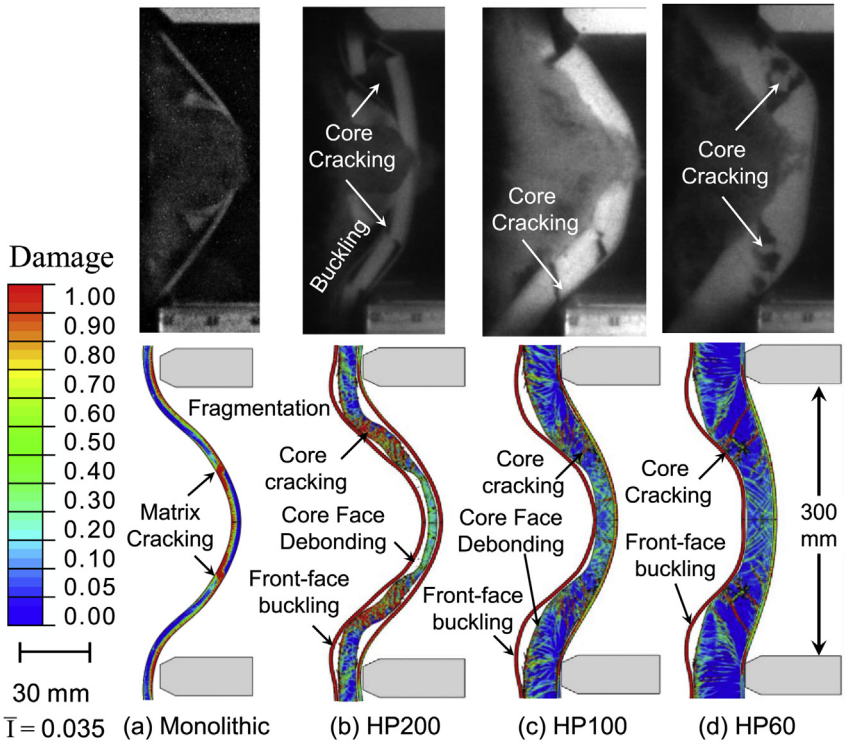

Fig. 17. Cross-sectional view showing the distribution of core and facesheet damage in air-backed (a) monolithic composite and (b–d) sandwich structures with HP60, HP100 and HP200 cores. The calculated orientations and locations of failure mechanisms in the face, core and at core–face interfaces are in reasonable agreement with experimental observations. Projectile velocity is 75 m s^{-1} and $\bar{I} = 0.035$.

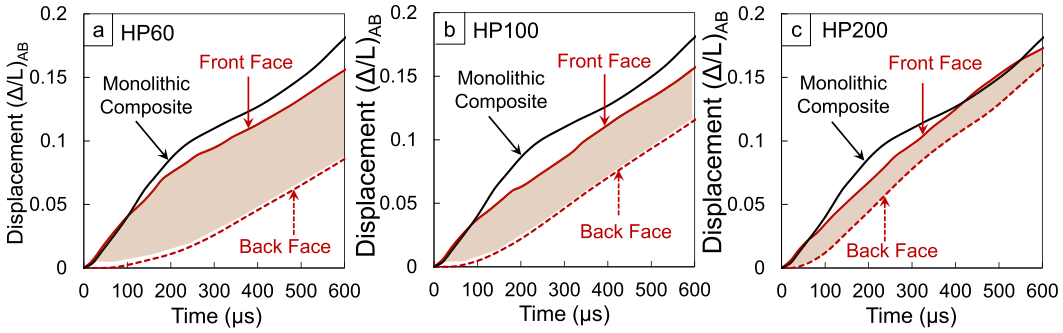

Fig. 18. Front and back-face displacements as functions of time for air-backed sandwich structures with (a) HP200, (b) HP100, and (c) HP60 cores subjected to $\bar{I} = 0.035$. The shaded region is the core compression in each case. The solid black line denotes the displacement of the monolithic composite.

spreading capacities of the core are critical for enhancing blast resistance.

Significant deformation in the backface follows core crushing and load transfer through the core. The higher the rate of deformation in the backface, the lower is the blast mitigation capability of the composite. For the HP200 core, the displacement in the backface occurs after a delay of ~50 μs. Comparison of the deflections for front and backfaces shows that both faces move with similar velocities. The backface deflection for this case is ~90% of the deflection in the monolithic composite. For the HP100 core, the displacement in the backface occurs after a delay of ~75 μs and the backface experiences ~70% of the displacement in the monolithic composite. For the HP60 core, displacement in the backface occurs after a delay of ~100 μs and the backface deflection is ~40% of the deflection in monolithic composite. The shaded regions in the plots show the core compression for each case. As the relative core density increases, core compression decreases significantly. A comparison of the slopes of the front and backface displacement vs. time plots indicates that thicker, low-density cores provide the greatest reduction in frontface velocity and the longest delay after the onset of loading for structural deflection to initiate. Fig. 19 shows the normalized deflection (Δ/L) as a function of impulse $\bar{I}$ for structures with different relative densities. A monotonically increasing trend of center deflections with increasing core density is observed and shows reasonable agreement with experimental observations. At all impulse magnitudes, structures with the lowest relative density experience the least deflections. The deflections

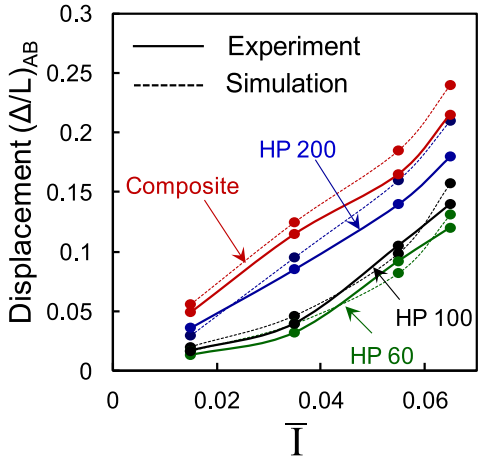

Fig. 19. Comparison of experimentally measured and numerically calculated mid-plane deflections at 1000 μs in air-backed structures as functions of normalized incident impulse $\bar{I}$ for different normalized core densities. The results from experiments are in good agreement with those obtained from finite element simulations.

increase with increasing relative density and impulse magnitudes. The structure with the HP200 core performs only marginally better than monolithic structures. The HP100 and HP60 cores yield significantly higher blast resistances in comparison to the HP200 core and the monolithic composite.

7.3. Impulse transmission

Minimizing the impulse transmitted to the internal components of marine vessels is of critical importance. For the simply-supported loading configuration discussed here, the target structure transmits an impulse to the supports. The rate of impulse transmission and the magnitude of the transmitted impulse can provide valuable insight into the blast resistance and performance of composite structures. Clearly, the composite structure that transmits the least impulse at the lowest rate is most desirable. Fig. 20(a)–(d) shows the histories of impulses transmitted by air-backed structures subjected to incident impulsive loads of different magnitudes. It can be seen that, compared to the monolithic composite plate, the sandwich structures transmit significantly lower impulses and at much lower rates. In particular, the structure with the HP200 core shows a marked improvement in blast resistance over the monolithic panel. As the core density decreases and the corresponding core thickness increases, the improvements in blast mitigation are more noticeable. For example, for an incident impulse magnitude of $\bar{I} = 0.065$ ($I = 0.42$ kPa s) shown in Fig. 20(d), the sandwich structures with HP200, HP100 and HP60 cores transmit ~40%, 30% and 20% of the impulse transmitted by the monolithic composite, respectively. Correlating the rate of impulse transmission with the core characteristics in each case shows that, as the core density decreases and core thickness increases correspondingly, the rate of impulse transmission decreases significantly. The peak transmitted impulse as a function of incident impulses and core densities is plotted in Fig. 21. For each sandwich structure, the impulses transmitted are significantly lower than those for the monolithic composite. The transmitted impulses increase exponentially with increasing relative density $\bar{I} = 0.065$ and increase monotonically with the increasing incident impulse. The experiments and simulations reveal that the sandwich core is essential for spreading the load uniformly over the entire span of the structure and absorbing the incident impulsive loads to enhance the blast mitigation capabilities of the structures.

Fig. 21 shows the transmitted impulse for air-backed structures $(I_T)_{AB}$ for all 16 configurations as a function of normalized incident impulse $\bar{I}$ and normalized relative density $\bar{\rho}$. At all impulse magnitudes, structures with the lowest relative density transmit the least impulse. The transmitted impulse increases with increasing relative density as well as impulse magnitude. HP200 cores

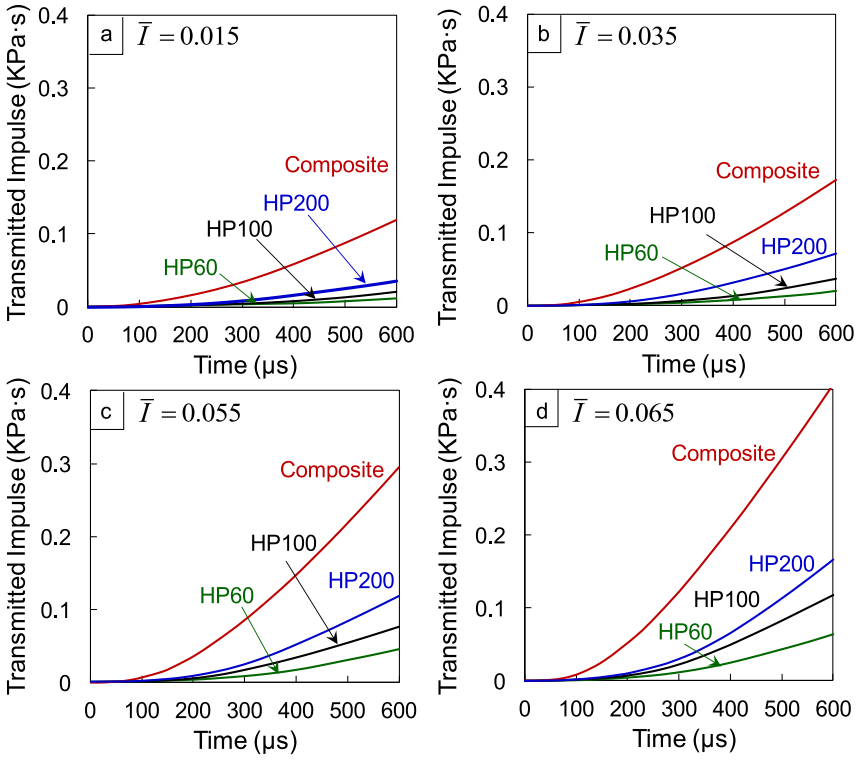

Fig. 20. Impulse transmitted to the supports for air-backed composites as function of time for different incident impulsive loads.

perform better than monolithic structures while HP100 and HP60 cores exhibit significantly higher blast mitigation in comparison to HP200 core and the monolithic composite. The relationship between deflection in air-backed structures $(I_T)_{AB}$, and $\bar{I}$ and $\bar{\rho}$ can be given by

$$(I_T)_{AB} = 100 \cdot \bar{\rho}^{(1.8)} \cdot \bar{I}^{(1.03)}. \tag{23}$$

7.4. Response of water-backed structures

An analysis of structural performance in water-backed conditions is important for the design of critical parts of ship structures like turbine blades, hull and keel. Water-backed conditions also prevail in underwater pipelines and ducts. Moreover, a number of sections in the hull of a marine vessel are backed by movable equipment and machinery which creates conditions similar to water-backed loading conditions. In addition to the results for air-backed structures reported so far, an additional set of simulations is carried out to investigate the role of water in contact with both sides of the structure. The load configuration for this case is shown in Fig. 3(b). Fig. 22 shows the distributions of damage in four different composite structures in water-backed loading for $\bar{I} = 0.035$. These contour plots illustrate the differences in the behavior of air-backed and water-backed structures. For the monolithic composite, high shear stresses develop near the circumference of the loaded area, causing severe damage in the form of matrix cracking. For the sandwich structures, however, flexural waves in the frontface cause core frontface debonding and frontface buckling. Damage is localized and the structure is relatively undamaged in regions that are away from the loading area. Clearly, for all structures, the overall deflection under water-backed conditions is severely restricted due to the presence of the back side water. Due to the lack of overall deflection and bending, tensile loads in both faces are negligible and the faces undergo significantly lower amount of damage in comparison to the corresponding air-backed cases.

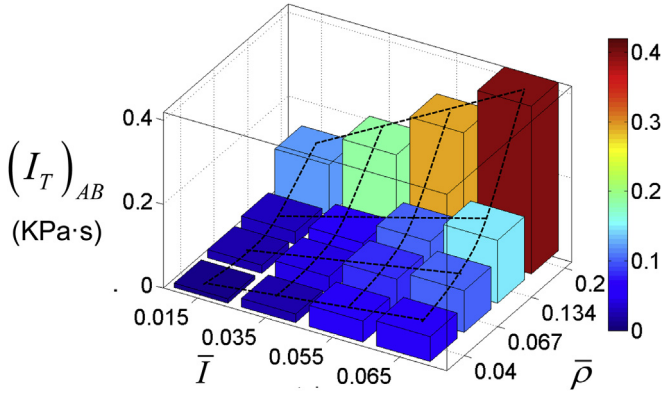

Fig. 21. Transmitted impulse in air-backed structures as function of normalized incident impulse $\bar{I}$ and normalized density $\bar{\rho}$.

To evaluate the role of relative density on dynamic response, the histories of center displacements experienced by the monolithic composite and both faces in the sandwich structures are shown in Fig. 23. The shaded region illustrates the core compression. Core compressive strains for all cores are similar (~100%), but the absolute core compression is significantly higher for HP60 than for HP100 and HP200. For the sandwich structures, due to low relative core densities, the frontface starts to move with a higher velocity than the monolithic plate and the frontface velocity is limited by the core. Therefore, the momentum transferred to the core increases with increasing relative core density. Fig. 24 shows the normalized deflections (Δ/L) for all 16 cases for the water-backed case as a function of impulse $(\bar{I})$. As observed in air-backed

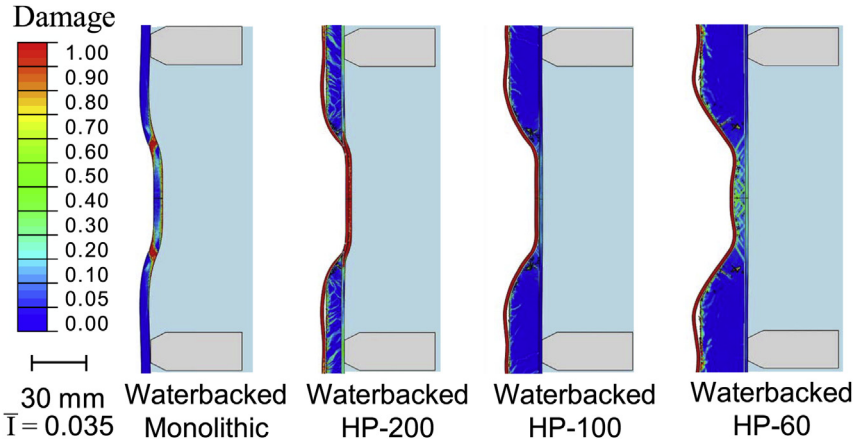

Fig. 22. Distributions of damage in water-backed monolithic composite and sandwich structures with HP60, HP100 and HP200 cores. Deformation is highly localized due to the presence of back side water section which affects both deflection and impulse transmission. Design of such structures requires different considerations than air-backed structures. Projectile velocity is 75 m s^{-1} and $\bar{I} = 0.035$.

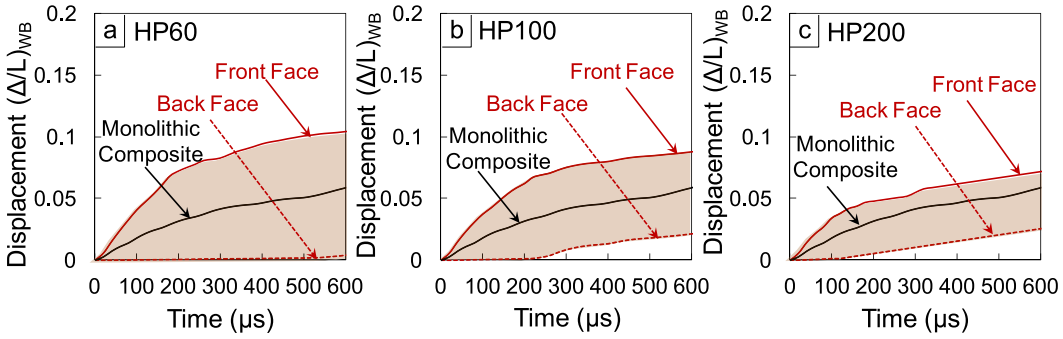

Fig. 23. Front and backface displacements as functions of time for water-backed sandwich structures with (a) HP60, (b) HP100, and (c) HP200 cores subjected to an impulse of $\bar{I} = 0.035$. The shaded region is the core compression in each case. The solid black line denotes the displacement of the monolithic composite.

structures, thick cores with low relative density provide the best blast mitigation. In the water-backed case, on average, the deflections are 50% of the deflections in the air-backed case.

Fig. 24 shows the transmitted impulse $(\Delta/L)_{WB}$ for all 16 cases as a function of normalized incident impulse $\bar{I}$ and normalized relative density $\bar{\rho}$. The vertical axis shows the normalized deflection $(\Delta/L)_{WB}$. At all impulse magnitudes, the magnitude of the transmitted impulse increases monotonically with the relative density. As the core density increases, the fraction of incident impulse transmitted by the structure in a water-backed configuration also increases significantly. The relationship between deflection in water-backed structures $(\Delta/L)_{AB}$, and $\bar{I}$ and $\bar{\rho}$ can be given by

$$(\Delta/L)_{WB} = 20 \cdot \bar{\rho}^{(0.36)} \cdot \bar{I}^{(1.60)}. \quad (24)$$

The resistance of a water-backed structure to applied impulse can be quantified by the magnitude of the impulse transmitted into the back side water section. Fig. 25 shows the histories of transmitted impulses for water-backed composite structures subjected to similar impulsive loads. The pressure pulses in the back side water section are measured and the corresponding impulses are calculated using eqn. (2). In all cases, the monolithic composite exhibits the least blast mitigation and transmits more than ~80% of the incident impulse into the back side water section. The HP200 core transmits ~40% of the incident impulse. During and up to the

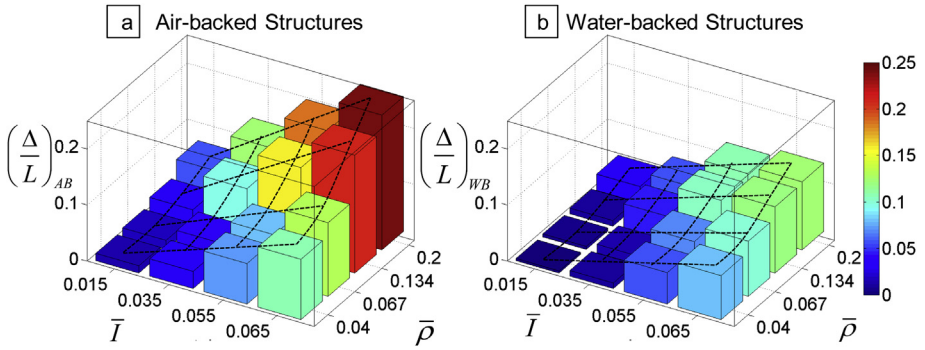

Fig. 24. Normalized mid-plane deflection in air-backed and water-backed structures as function of normalized incident impulse $\bar{I}$ and normalized density $\bar{\rho}$.

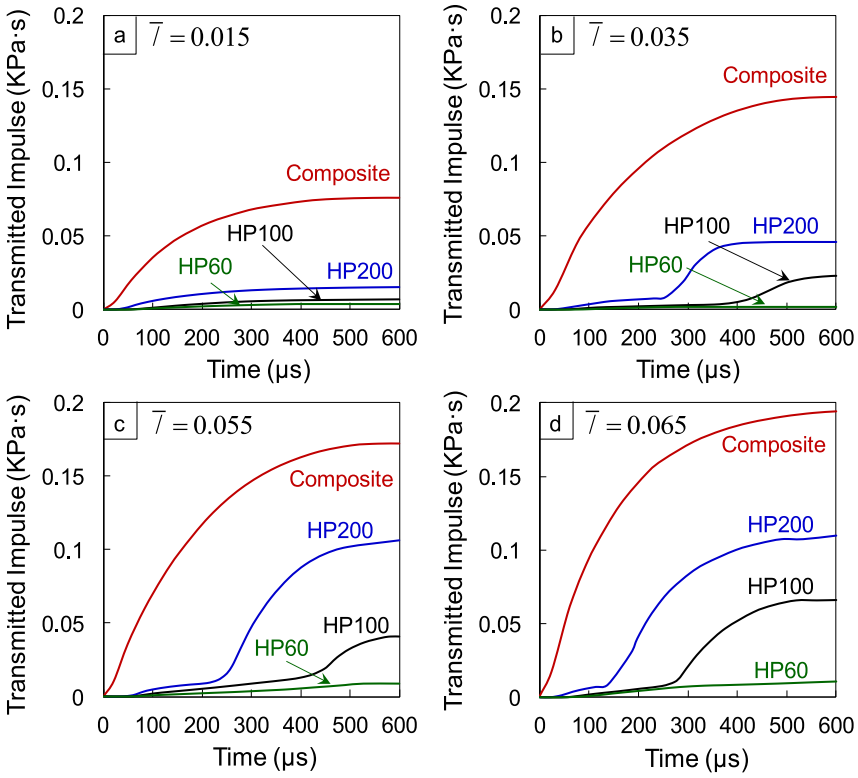

Fig. 25. Impulse transmitted to the rear water-section for water-backed composites as function of time for different incident impulses.

core compression stage, or at approximately 100 μs, the impulse transmitted is very low. However, when the core fails completely (at ~400 μs), the frontface "slaps" into the backface and both faces start to move together, causing a pressure pulse to be generated and transmitted into the back side water. The structure with the HP100 core transmits ~20% of the incident impulse with a low pressure plateau followed by complete impulse at the end of 600 μs. Clearly, blast mitigation in water-backed conditions is relatively insensitive to face thickness and is highly dependent on core density and thickness. The histories of transmitted impulses show that the rate of impulse transmission is highly dependent on the core density. For instance, in Fig. 25(d), the monolithic composite transmits the impulse almost instantaneously after the onset of loading while in the sandwich structure, the transmission of the impulse is controlled by core crushing and the impulse is transmitted after complete core collapse. The time duration for failure in each sandwich structure can be clearly identified by the steep rise in transmitted impulse.

Fig. 26 shows the transmitted impulse $(I_T)_{WB}$ for all 16 cases as a function of normalized incident impulse $\bar{I}$ and normalized relative density $\bar{\rho}$. The vertical axis shows the transmitted impulse (I_T). At all impulse magnitudes, the magnitude of the transmitted impulse increases monotonically with the relative density. As the core density increases, the fraction of incident impulse transmitted by the structure in a water-backed configuration also increases significantly. The relationship between transmitted impulse in water-backed structures$(I_T)_{WB}$, and $\bar{I}$ and $\bar{\rho}$ can be given by

$$(I_T)_{WB} = 100 \cdot \bar{\rho}^{(2.1)} \cdot \bar{I}^{(1)}. \tag{25}$$

8. Conclusions

Marine structures must balance strength and load carrying capacity with the ability to minimize impulse transmission for high blast and impact resistance. Composite structures have higher stiffnesses and high strength-to-weight ratios compared with monolithic structures. Additionally, sandwich structures provide very high bending and shear resistances with slight increases in total mass. However, due to the novelty and wide range of structural combinations, the relationships between structural responses and material heterogeneity in sandwich structures are not well quantified. In particular, the behavior of composite structures under extreme impulsive loading generated by underwater explosions needs to be systematically analyzed. In an effort to provide useful information for structural design, the load carrying capacity and impulse transmission capabilities of sandwich composites are evaluated over a range of relative densities and impulsive load intensities. The loading conditions involve impulsive loads with peak pressures up to 200 MPa, which simulate the effects of TNT

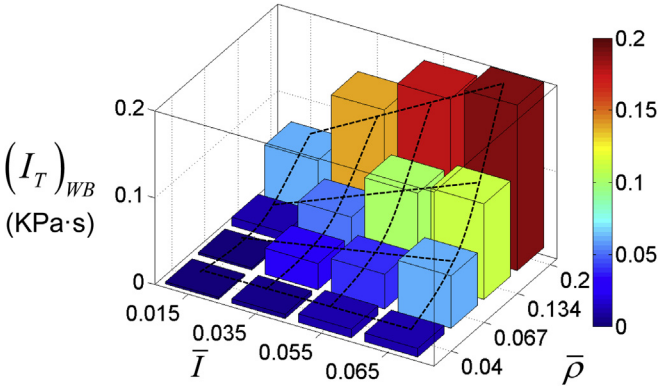

Fig. 26. Transmitted impulse in water-backed structures as function of normalized incident impulse $\bar{I}$ and normalized density $\bar{\rho}$.

exploding underwater at different standoff distances from the structure. The constitutive and damage models capture the different inelastic deformation and failure mechanisms in composite laminates and sandwich cores. It should be emphasized that the composite panels studied have similar overall mass which necessitates different core thicknesses. The effect of core height on dynamic response is not studied in this analysis.

This study has yielded experimental data on the failure behavior of composites subjected to underwater impulses. Maximal damage was observed near the load circumference in both monolithic and sandwich structures. The analysis of damage modes shows that relative core density is a critical factor in determining structural performance of sandwich structures. Sandwich structures significantly outperform monolithic composites at all impulsive levels and environmental conditions. Low density cores provide higher blast resistance than high density cores. An analysis of the effect of load intensity shows that as the load intensity increases, the deflection of the frontface outpaces the dynamic core crushing capability of the cores, resulting in collapse. In such cases, low density cores provide better load spreading and exhibit better capabilities for compression. However, a major concern for low density cores is the occurrence of core indentation, in which the core fails in a localized region and causes compressive stresses in the frontface leading to buckling and rupture. Therefore, a balance of core stiffness and softness is essential for optimal blast resistance.

Comparison of experiments and simulations shows that numerical calculations provide a reasonable representation of damage and dissipation mechanisms in the facesheets and core. The compressible foam constitutive model leads to high core compression and a slight overestimate of backface deflection. The finite element model captures the essential deformation mechanisms observed in both the facesheets and the core. Specifically, the following deformation modes are replicated with reasonable accuracy: core indentation, core shear, core–face debonding, facesheet buckling and delamination, structural collapse and rupture. The results from numerical calculations provide a more in-depth understanding of temporal and spatial evolution of different deformation modes in the structure. The deformation in sandwich structures is strongly influenced by core density and loading rate and magnitude. Structures with high relative densities undergo severe damage and exhibit significantly higher core face debonding than structures with low relative densities. For a given impulsive load, structures with low relative densities (HP60 and HP100) experience considerably lower displacements than those with high relative densities (HP200 and monolithic).

In both air-backed and water-backed cases, the maximum impulse transmitted by each structure is used to determine the performance of the composite structure. Sandwich structures exhibit superior blast mitigation capabilities in comparison to monolithic structures at all impulse magnitudes. In particular, thick, low density foam cores made of Divinycell HP60 and HP100 foams provide the highest load spreading and impulse retardation. The temporal histories of impulse transmission show a significant dependence on core density with a clear increase in transmitted impulse after complete core failure. The transmitted impulses show a monotonic dependence on loading intensity and a power law dependence on the relative density. The effects of high relative density are further exacerbated at higher loading intensities.

Based on parametric calculations, empirical relations are obtained to quantify structural performance in terms of deflection and impulse transmission as a function of load (air-backed or water-backed, load intensity) and material attributes. These relations are summarized in Table 5. The insight gained here provides guidelines for the design of structures for which response to water based impulsive loading is an important consideration. Finally, it should be noted that the relations described in this paper are applicable only for the structural attributes and loading conditions considered herein.

Table 5
Summary of material–structure–property relationships.

	Air-backed	Water-backed
Deflection	$(\Delta/L)_{AB} = 20\cdot\bar{p}^{(0.62)}\cdot\bar{I}^{(1.20)}$.	$(\Delta/L)_{WB} = 20\cdot\bar{p}^{(0.36)}\cdot\bar{I}^{(1.60)}$.
Impulse transmission	$(I_T)_{AB} = 100\cdot\bar{p}^{(1.8)}\cdot\bar{I}^{(1.03)}$.	$(I_T)_{WB} = 100\cdot\bar{p}^{(2.1)}\cdot\bar{I}^{(1)}$.

Acknowledgment

Support by the Office of Naval Research through grant numbers N00014-09-1-0808 and N00014-09-1-0618 (program manager: Dr. Yapa D. S. Rajapakse) is gratefully acknowledged. Calculations are carried out on the Athena HPC cluster in the Dynamic Properties Research Laboratory at Georgia Tech. MZ also acknowledges beneficial interactions through the CAS/SAFEA International Partnership Program for Creative Research Teams.

References

[1] Abrate S. Impact on laminated composite materials. Appl Mech Rev 1991;44(4):155–90.
[2] Abrate S. Impact on laminated composites: recent advances. Appl Mech Rev 1994;47:517–44.
[3] Joshi SP, Sun CT. Impact induced fracture in a laminated composite. J Compos Mater 1985;19:51–66.
[4] Chang FK, Choi HY, Jeng ST. Study on impact damage in laminated composites. Mech Mater 1990;10:83–95.
[5] Chang FK, Choi HY, Jeng ST. Characterization of impact damage in laminated composites. Sampe J 1990;26:18–25.
[6] Lessard LB, Chang FK. Damage tolerance of laminated composites containing an open hole and subjected to compressive loadings .2. Experiment. J Compos Mater 1991;25:44–64.
[7] Cantwell WJ, Morton J. The impact resistance of composite-materials – a review. Composites 1991;22:347–62.
[8] Hashin Z. Analysis of stiffness reduction of cracked cross-ply laminates. Eng Fract Mech 1986;25:771–8.
[9] Hashin Z. Analysis of orthogonally cracked laminates under tension. J Appl Mech-T ASME 1987;54:872–9.
[10] Minnaar K, Zhou M. A novel technique for time-resolved detection and tracking of interfacial and matrix fracture in layered materials. J Mech Phys Solids 2004;52:2771–99.
[11] Hashin Z. Failure criteria for unidirectional fiber composites. J Appl Mech-Trans ASME 1980;47:329–34.
[12] Fatt MSH, Palla L. Analytical modeling of composite sandwich panels under blast loads. J Sandw Struct Mater 2009;11:357–80.
[13] Mines RAW, Worrall CM, Gibson AG. The static and impact behavior of polymer composite sandwich beams. Composites 1994;25:95–110.
[14] Abot JL, Daniel IM. Composite sandwich beams under low velocity impact. In: Collection of Technical Papers – AIAA/ASME/ASCE/AHS/ASC Structures, Structural Dynamics and Materials Conference, vol. 1; 2001. p. 67–77. Seattle, WA.
[15] Tagarielli VL, Deshpande VS, Fleck NA. The high strain rate response of PVC foams and end-grain balsa wood. Compos Part B-Eng 2008;39:83–91.
[16] Qiao PZ, Yang MJ, Bobaru F. Impact mechanics and high-energy absorbing materials: review. J Aerosp Eng 2008;21:235–48.
[17] Lee S, Barthelat F, Moldovan N, Espinosa HD, Wadley HNG. Deformation rate effects on failure modes of open-cell Al foams and textile cellular materials. Int J Solids Struct 2006;43:53–73.
[18] Zhang J, Kikuchi N, Li V, Yee A, Nusholtz G. Constitutive modeling of polymeric foam material subjected to dynamic crash loading. Int J Impact Eng 1998;21:369–86.
[19] Deshpande VS, Fleck NA. Isotropic constitutive models for metallic foams. J Mech Phys Solids 2000;48:1253–83.
[20] Steeves CA, Fleck NA. Collapse mechanisms of sandwich beams with composite faces and a foam core, loaded in three-point bending. Part II: experimental investigation and numerical modelling. Int J Mech Sci 2004;46:585–608.
[21] Tagarielli VL, Deshpande VS, Fleck NA. The dynamic response of composite sandwich beams to transverse impact. Int J Solids Struct 2007;44:2442–57.
[22] Schubel PM, Luo JJ, Daniel IM. Impact and post impact behavior of composite sandwich panels. Compos Part A-Appl Sci Manuf 2007;38:1051–7.

[23] Nemes JA, Simmonds KE. Low-velocity impact response of foam-core sandwich composites. J Compos Mater 1992;26:500–19.
[24] I.M.D., Abot JL. Composite sandwich beams under low velocity impact. In: Proc. of AIAA Conf.; 2001. Seattle.
[25] Schubel PM, Luo JJ, Daniel IM. Low velocity impact behavior of composite sandwich panels. Composites Part A-Appl Sci Manuf 2005;36:1389–96.
[26] Liang YM, Spuskanyuk AV, Flores SE, Hayhurst DR, Hutchinson JW, McMeeking RM, et al. The response of metallic sandwich panels to water blast. J Appl Mech-Trans ASME 2007;74:81–99.
[27] Dharmasena KP, Queheillalt DT, Wadley HNG, Dudt P, Chen Y, Knight D, et al. Dynamic compression of metallic sandwich structures during planar impulsive loading in water. Eur J Mech A-Solids 2010;29:56–67.
[28] Wei Z, Deshpande VS, Evans AG, Dharmasena KP, Queheillalt DT, Wadley HNG, et al. The resistance of metallic plates to localized impulse. J Mech Phys Solids 2008;56:2074–91.
[29] Xue ZY, Hutchinson JW. Preliminary assessment of sandwich plates subject to blast loads. Int J Mech Sci 2003;45:687–705.
[30] Xue ZY, Hutchinson JW. A comparative study of impulse-resistant metal sandwich plates. Int J Impact Eng 2004;30:1283–305.
[31] Hutchinson JW, Xue ZY. Metal sandwich plates optimized for pressure impulses. Int J Mech Sci 2005;47:545–69.
[32] Qiu X, Deshpande VS, Fleck NA. Finite element analysis of the dynamic response of clamped sandwich beams subject to shock loading. Eur J Mech A-Solids 2003;22:801–14.
[33] Fleck NA, Deshpande VS. The resistance of clamped sandwich beams to shock loading. J Appl Mech-Trans ASME 2004;71:386–401.
[34] Qiu X, Deshpande VS, Fleck NA. Dynamic response of a clamped circular sandwich plate subject to shock loading. J Appl Mech-Trans ASME 2004;71:637–45.
[35] Hutchinson JW. Energy and momentum transfer in air shocks. J Appl Mech-Trans ASME 2009;76.
[36] Kambouchev N, Radovitzky R, Noels L. Fluid-structure interaction effects in the dynamic response of free-standing plates to uniform shock loading. J Appl Mech-Trans ASME 2007;74:1042–5.
[37] Deshpande VS, Fleck NA. One-dimensional response of sandwich plates to underwater shock loading. J Mech Phys Solids 2005;53:2347–83.
[38] Vaziri A, Hutchinson JW. Metal sandwich plates subject to intense air shocks. Int J Solids Struct 2007;44:2021–35.
[39] Espinosa HD, Lee S, Moldovan N. A novel fluid structure interaction experiment to investigate deformation of structural elements subjected to impulsive loading. Exp Mech 2006;46:805–24.
[40] Latourte F, Gregoire D, Zenkert D, Wei XD, Espinosa HD. Failure mechanisms in composite panels subjected to underwater impulsive loads. J Mech Phys Solids 2011;59:1623–46.
[41] Wei XD, de Vaucorbeil A, Tran P, Espinosa HD. A new rate-dependent unidirectional composite model – application to panels subjected to underwater blast. J Mech Phys Solids 2013;61:1305–18.
[42] McShane GJ, Stewart C, Aronson MT, Wadley HNG, Fleck NA, Deshpande VS. Dynamic rupture of polymer-metal bilayer plates. Int J Solids Struct 2008;45:4407–26.
[43] Dharmasena KP, Wadley HNG, Xue ZY, Hutchinson JW. Mechanical response of metallic honeycomb sandwich panel structures to high-intensity dynamic loading. Int J Impact Eng 2008;35:1063–74.
[44] Tekalur SA, Bogdanovich AE, Shukla A. Shock loading response of sandwich panels with 3-D woven E-glass composite skins and stitched foam core. Compos Sci Technol 2009;69:736–53.
[45] Tekalur SA, Shukla A, Shivakumar K. Blast resistance of polyurea based layered composite materials. Compos Struct 2008;84:271–81.
[46] LeBlanc J, Shukla A, Rousseau C, Bogdanovich A. Shock loading of three-dimensional woven composite materials. Compos Struct 2007;79:344–55.
[47] Grogan J, Tekalur SA, Shukla A, Bogdanovich A, Coffelt RA. Ballistic resistance of 2D and 3D woven sandwich composites. J Sandw Struct Mater 2007;9:283–302.
[48] Wang EH, Gardner N, Shukla A. The blast resistance of sandwich composites with stepwise graded cores. Int J Solids Struct 2009;46:3492–502.
[49] Arora H, Hooper P, Dear JP. Blast and other high rate loading composite sandwich materials. In: Ravichandran G, editor. 9th International Conf on Sandwich Structures (ICSS-9). Pasedena, USA: California Institute of Technology; June 2010. Key-note paper MA3.1.
[50] Arora H, Hooper PA, Dear JP. The effects of air and underwater blast on composite sandwich panels and tubular laminate structures. Exp Mech 2012;52:59–81.
[51] Langdon GS, Karagiozova D, von Klemperer CJ, Nurick GN, Ozinsky A, Pickering EG. The air-blast response of sandwich panels with composite face sheets and polymer foam cores: experiments and predictions. Int J Impact Eng 2013;54:64–82.
[52] Langdon GS, von Klemperer CJ, Rowland BK, Nurick GN. The response of sandwich structures with composite face sheets and polymer foam cores to air-blast loading: preliminary experiments. Eng Struct 2012;36:104–12.
[53] Avachat S, Zhou M. Effect of facesheet thickness on dynamic response of composite sandwich plates to underwater impulsive loading. Exp Mech 2011;52:83–93.
[54] S. Avachat, M. Zhou, Dynamic response of composite sandwich structures subjected to underwater impulsive loads: Experiments and Simulations Conference Proceedings of the 16th International Conference on Composite Structures, ICCS-16, A.J.M. Ferreira (Editor), FEUP, Porto, 2011, (2011).
[55] Avachat S, Zhou M. Dynamic response of submerged composite sandwich structures to blast loading. In: Shukla A, editor. IMPLAST 2010-SEM Fall Conference. Providence, Rhode Island, USA: Society for Experimental Mechanics, Inc.; 2010.
[56] Wei XD, Tran P, de Vaucorbeil A, Ramaswamy RB, Latourte F, Espinosa HD. Three-dimensional numerical modeling of composite panels subjected to underwater blast. J Mech Phys Solids 2013;61:1319–36.
[57] Swisdak MM. Explosion effects and properties: Part II – explosion effects in water. Technical Report. Dahlgren, Virginia, USA: Naval Surface Weapons Center; 1978.
[58] Taylor GI. The pressure and impulse of submarine explosion waves on plates. In: The scientific papers of G I Taylor, vol. III. Cambridge: Cambridge University Press; 1941. p. 287–303.
[61] S.D. DIAB Inc., DeSoto, Texas 75115, USA http://www.diabgroup.com/europe/literature/e_pdf_files/man_pdf/H_man.pdf [accessed 5.05.11].
[62] Latourte F, Wei XD, Feinberg ZD, de Vaucorbeil A, Tran P, Olson GB, et al. Design and identification of high performance steel alloys for structures subjected to underwater impulsive loading. Int J Solids Struct 2012;49:1573–87.
[63] Battley M, Allen T. Servo-hydraulic system for controlled velocity water impact of marine sandwich panels. Exp Mech 2012;52:95–106.
[64] Wadley HNG, Borvik T, Olovsson L, Wetzel JJ, Dharmasena KP, Hopperstad OS, et al. Deformation and fracture of impulsively loaded sandwich panels. J Mech Phys Solids 2013;61:674–99.
[65] Dharmasena KP, Wadley HNG, Williams K, Xue ZY, Hutchinson JW. Response of metallic pyramidal lattice core sandwich panels to high intensity impulsive loading in air. Int J Impact Eng 2011;38:275–89.
[66] Michael J. Phys Rev B 1993;47:2493.
[67] Mori LF, Lee S, Xue ZY, Vaziri A, Queheillalt DT, Dharmasena KP, et al. Deformation and fracture modes of sandwich structures subjected to underwater impulsive loads. J Mech Mater Struct 2007;2:1981–2006.
[68] Hibbit, Karlsson, Sorensen. Abaqus/explicit user's manual. Version 6.9. 2009.
[69] Lapczyk I, Hurtado JA. Progressive damage modeling in fiber-reinforced materials. Compos Part A-Appl Sci Manuf 2007;38:2333–41.
[70] Daniel IM, Ishai O. Engineering mechanics of composite materials. New York: Oxford University Press; 2006.
[71] Daniel IM, Luo JJ, Schubel PM, Werner BT. Interfiber/interlaminar failure of composites under multi-axial states of stress. Compos Sci Technol 2009;69:764–71.
[72] Roy R, Sarkar BK, Bose NR. Impact fatigue of glass fibre-vinylester resin composites. Compos Part A-Appl Sci Manuf 2001;32:871–6.
[73] Compston P, Jar PYB, Davies P. Matrix effect on the static and dynamic interlaminar fracture toughness of glass-fibre marine composites. Compos Part B-Eng 1998;29:505–16.
[74] S.D. DIAB Inc., DeSoto, Texas 75115, USA.
[75] Deshpande VS, Fleck NA. Multi-axial yield behaviour of polymer foams. Acta Mater 2001;49:1859–66.
[76] Hooputra H, Gese H, Dell H, Werner H. A comprehensive failure model for crashworthiness simulation of aluminium extrusions. Int J Crashworthines 2004;9:449–63.
[77] Poapongsakorn P, Carlsson LA. Fracture toughness of closed-cell PVC foam: effects of loading configuration and cell size. Compos Struct 2013;102:1–8.
[78] Triantafillou TC, Gibson LJ. Failure mode maps for foam core sandwich beams. Mater Sci Eng 1987;95:37–53.
[79] Triantafillou TC, Zhang J, Shercliff TL, Gibson LJ, Ashby MF. Failure surfaces for cellular materials under multiaxial loads .2. Comparison of models with experiment. Int J Mech Sci 1989;31:665–78.

Further reading

[1] Taylor GI. The scientific papers of G I Taylor. Cambridge: Cambridge University Press; 1963.
[2] Cole RH. Spherical shock waves from underwater explosions. Phys Rev 1947;72.177–177.